Physica D 467 (2024) 134263

Contents lists available at ScienceDirect

Physica D

journal homepage: www.elsevier.com/locate/physd

Baroclinic vortex pulsars in unstable westward flows

Pavel Berloff [a,b,*], Georgi G. Sutyrin [c]

[a] *Department of Mathematics, Imperial College London, London, United Kingdom*
[b] *Institute of Numerical Mathematics, Russian Academy of Sciences, Moscow, Russia*
[c] *Graduate School of Oceanography, University of Rhodes Island, Narragansett, USA*

ARTICLE INFO

Communicated by Dmitry Pelinovsky

Keywords:
Nonlinear coherent vortices
Geophysical fluid dynamics
Baroclinic flows

ABSTRACT

We present a computational modeling study of geophysical coherent vortices embedded in horizontally homogeneous, baroclinically unstable, westward background flows with vertical shear. Within an idealized two-layer quasigeostrophic beta-plane model, we discovered two types of robust vortex-wave structures with distinct properties, which remain asymmetric and nonstationary in statistically-equilibrated turbulent flow regimes. The corresponding vortices, referred to as *baroclinic vortex pulsars*, are characterized by intense vorticity core coupled to the Rossby wave wake. The main conclusion — on the top of various analyses discussed in the paper — are that the vortex pulsars are fundamentally *non-isolated* coherent vortices, because they extract energy from the background circulation and expel excess potential vorticity, accumulating due to down-gradient material propagation, back into the environment. Both types may coexist as multiple statistically equilibrated states in some range of physical parameters, complicating any parameterization of eddy effects in climate-type models.

1. Introduction

Coherent vortices are ubiquitous in geophysical, that is, rotating and stratified, fluids, such as oceans and planetary atmospheres (e.g., [1] McWilliams and Weiss 1994). The background literature on this phenomenon is large and includes observational evidence (e.g., [2] Dowling and Spiegel 1990), numerical modeling results (e.g., [3] McWilliams 1984), laboratory experiments (e.g., [4] Brown and Roshko 1974) and analytical solutions (e.g., [5] Larichev and Reznik 1976). The vortices are crucially affected by the large-scale ambient potential vorticity (PV) distribution, which in turn is shaped up by the planetary beta-effect, large-scale flow and stratification patterns, and by the bottom topography. The vortices provide various effects, but most importantly long-distance transport mechanisms for various material and dynamically important properties. In turn, these effects and mechanisms impact and alter large-scale oceanic general circulation, which globally affects the whole Earth system. Within this larger scope and context, coherent vortices can be viewed as a type of mesoscale oceanic eddies. This type is important phenomenon and big research challenge (e.g., [6] McWilliams 2008; [7] Chelton et al. 2011). Further below, after briefly discussing what "coherent" means in the context, we will drop this adjective out for brevity.

An exact definition of a vortex is elusive, similarly to an attempting to define a wave. One of the approaches is to define the vortex boundary via the least deformable material line ([8] Haller et al. 2021), but one might argue that this defines only the isolated vortex core, whereas significant part of the surrounding flow field should also belong to the vortex. Typical vortices are both localized in space and persistent in time relative vorticity concentrations in the surrounding turbulent field characterized by much weaker vorticity anomalies, which undergo forward cascade of enstrophy towards its destruction by dissipation on the smallest scales. The spatial localization of a coherent vortex corresponds to some non-random distribution of the Fourier phases, hence, to global correlations in the wavenumber spectrum. Overall, existence of coherent vortices contradicts common view of turbulence as a local spectral cascade ([3] McWilliams 1984).

Vortices have different shapes (e.g., monopoles and dipoles), interact with each other and ambient motions, and typically propagate due to various mechanisms. Even circular vortices do not have a unique functional form for the radial profiles; each profile is influenced by the history of interactions with other vortices and by the vortex generation mechanism. Vortices can be generated by various processes, most commonly by flow instabilities, and have different life cycles and termination mechanisms. Vortices can be persistent as quasi-stationary flow features, in the sense that for long time they do not necessarily need strong forcing to be maintained against various dissipative mechanisms. Nonstationarity of vortices can be due to interactions with ambient flow features and due to intrinsic dynamical processes in the vortex, such

* Correspondence to: Imperial College London, Department of Mathematics, Huxley Bldg., London, SW7 2AZ, United Kingdom.
E-mail address: p.berloff@imperial.ac.uk (P. Berloff).

https://doi.org/10.1016/j.physd.2024.134263
Received 10 March 2024; Received in revised form 8 June 2024; Accepted 12 June 2024
Available online 22 June 2024
0167-2789/

as instabilities and wave radiation. For example, common quadrupole perturbations of a circular symmetric vortex reflect existence, changes, and rotation of vortex ellipticity [3], which is often confirmed by the observations ([9] Chen et al. 2019). It is argued that pronounced deviations from circular symmetry are important for enhanced heat transport by the vortices ([10] Sutyrin, 2023; [11] Wang et al. 2023). A recent discussion of vortex dipoles, which is another common type, can be found in [12,13] Davies et al. (2023a,b).

Generation of the Rossby waves, which exist due to the background PV gradient (e.g., beta-effect), is recognized to be important for the vortex dynamics ([14] McWilliams and Flierl 1979). The beta-effect produces dipolar perturbations to a monopolar vortex, resulting in its persistent zonal and meridional propagations ([15] Sutyrin and Flierl 1994). Without a background flow, as vortices propagate meridionally (cyclones — poleward, anticyclones — equatorward), their PV anomaly extremum decreases, they leak out their PV content, can become unstable, get deformed and tend to decay by losing their energy into the lee Rossby wave wake ([16] Sutyrin et al. 1994; [17] Lam and Dritschel 2001). However, on longer time scales monopolar vortices may undergo an adjustment process and enter a slow-decaying quasi-stable state with nonzero meridional propagation, which depends on the vortex intensity ([18] Early et al. 2011). In principle, background general circulation may resupply a vortex with PV content and energy, to compensate for the leakage and dissipation ([19] Sutyrin and Radko 2021). However, such processes remain poorly understood; in fact, they are in the center of the reported results.

Next, let us compare *westward* background (WB) flows and *eastward* background (EB) flows, by which we refer to the flow directions in the upper ocean, assuming that they are vertically sheared towards zero velocity at the ocean bottom. In the simplest two-layer inviscid QG model ([20] Phillips 1954), the baroclinic flow instability is related to the sign change (in vertical) of the meridional PV gradient. This implies negative PV gradient either in the lower layer (EB case) or in the upper layer (WB case). Development and saturation of vortices in baroclinic turbulence were more often studied in EB flows, which represent Antarctic Circumpolar Current and atmospheric jetstreams (e.g., [21] Gallet and Ferrari 2020, and references therein). On the other hand, WB flows, which dominate most of the midlatitude ocean gyres, remain poorly studied. Important difference between statistically equilibrated eddy fields in EB and WB flows ([22] Berloff et al. 2011) is that an unstable WB flow (with negative PV gradient in the upper layer) generates more intense and long-lived coherent vortices than an unstable EB flow (with positive PV gradient in the upper layer). The systematic meridional propagation of vortices in the WB flow is such that cyclones move poleward and anticyclones move in the opposite direction. In this sense, the upper-ocean cyclonic PV anomaly propagates down the negative upper-ocean PV gradient, thus, resulting in its self-induced Lagrangian increase and subsequent enhancement of the vortex intensity — this basically follows from the angular momentum conservation. The corresponding WB vortex statistics and the involved physical mechanisms remain to be studied.[1] There is also solid observational evidence that WB flows tend to support more long-lived vortices ([23] Sangra et al. 2009; [24] Dalmahamod et al. 2018), but both taxonomy of these vortices and its relation to the background circulation patterns remain to be understood.

After focusing the present work on the unstable WB flows, let us now discuss its relevant theoretical precursors. Inviscid analytical solution for meridionally propagating baroclinic vortex with the attached lee Rossby wave wake (to be referred as simply "wake") was derived for the marginally stable WB flow ([25] Sutyrin et al. 2021a). This solution is characterized by energy transfer from the WB flow that compensates for the energy loss into the wake. The main feature of the wake is the opposite-sign vortex in the lower layer, that is shifted eastward relative to the upper-layer vortex core and, therefore, induces the meridional self-propagation mechanism and its dynamical consequences (see Fig. 1 in [26] Sutyrin et al. 2021b). Overall, this spatial pattern is similar to the self-propagating hetons ([27] Hogg and Stommel 1985) — referred so because of their efficiency in transporting heat anomalies — that are vortices with the opposite-sign PV anomalies in the upper and deep ocean. Note, that the hetons are essentially baroclinic dipoles forming from two opposite-sign vortices, without need for background PV gradient ([28] Gryanik et al. 2006), which is different in our case. The self-propagating vortex-wake features were found to emerge spontaneously in baroclinic turbulence developing on unstable WB flows ([26,29] Radko et al. 2022). Examples were tracked in both statistically steady equilibrium (if the eddy viscosity is large enough) and persistently intensifying regime (if the eddy viscosity is small). The later intensification can be stopped when vortices exit region of unstable WB flow ([30] Sutyrin et al. 2022). Note, that even subcritical WB flows help to maintain vortices and to increase their longevity ([31] Gulliver and Radko 2022). The present work continues the referenced research lines, but focuses on statistically equilibrated vortices and their fundamental properties.

Let us now discuss and justify the main elements of the selected problem set-up. First, it is essential that we consider evolution of vortices on unstable background flows, because in this case vortex-wave structures becomes naturally forced by the mean flow and, therefore, successfully resist dissipation and can reach a statistically equilibrated state (i.e., infinitely long life) with nearly steady propagation. An alternative way to reach final equilibrium might be by imposing some random or deterministic external forcing, however, not only physical grounds of this are hard to justify, but also unavoidable extra parameters will lead to unwieldy problem set-ups. Second, for the sake of initial simplicity, we deliberately consider dominant vortices, thus, leaving aside important mechanisms of vortex-vortex interactions, such as merger or cycling around of like-sign vortices ([32] Melander et al. 1988) and pairing of opposite-sign vortices into dipoles, which propagate for a while but eventually split apart (e.g., [12,13] Davies et al. 2023a,b). Third, we resort to high-resolution numerical modeling within framework of idealized, intermediate-complexity QG model with two-layer configuration, spatially homogeneous WB flow, flat bottom and doubly periodic domain. Fourth, we solve initial-value problems and pass over the long-time adjustment periods, as those considered earlier ([31] Gulliver and Radko 2022), in order to focus on the statistically equilibrated states corresponding to the stable attractors of the system.

The main objectives of our study are to obtain robust pulsating vortex-wave structures (pulsars) in statistically equilibrated regimes for a range of background flow intensities and other parameters, to analyze vortex shapes and propagation characteristics, and to extract the main dynamical balances. The paper is organized as the following: Section 2 explains the vortex model, Section 3 presents the main results, Section 4 discusses dependencies on the vertical shear and dissipative parameters, and Section 5 provides summary and discussion.

2. Numerical model

We chose the classical intermediate-complexity QG model to solve a set of initial-value problems and to reach statistically equilibrated states containing both pulsars and flow perturbations surrounding them, The governing QG PV equations for two dynamically active isopycnal layers, representing stratified and rotating, midlatitude open ocean, are:

$$\frac{\partial q_1}{\partial t} + J(\psi_1, q_1) + \beta\,\frac{\partial \psi_1}{\partial x} \;=\; \nu\nabla^4\psi_1\,, \qquad (1)$$

$$\frac{\partial q_2}{\partial t} + J(\psi_2, q_2) + \beta\,\frac{\partial \psi_2}{\partial x} \;=\; \nu\nabla^4\psi_2 - \gamma\nabla^2\psi_2\,, \qquad (2)$$

[1] It was though shown that these vortices are relatively unaffected by the latent, multiple, alternating zonal jets, also robustly emerging in this flow regime ([22] Berloff et al. 2011).

where subscript is the layer index starting from the top; x and y coordinates correspond to the eastward and poleward directions, respectively; $J(,)$ is the nonlinear Jacobian operator; and the terms with coefficients ν and γ are the (Newtonian) lateral eddy viscosity and the bottom friction, respectively. Isopycnal (i.e., layer-wise) PV anomalies q_i are related to the velocity streamfunctions ψ_i through the elliptic subproblem of PV inversion:

$$q_1 = \nabla^2\psi_1 + S_1(\psi_2 - \psi_1), \tag{3}$$

$$q_2 = \nabla^2\psi_2 + S_2(\psi_1 - \psi_2). \tag{4}$$

The layer-wise velocity components are found from the corresponding velocity streamfunctions:

$$u_i = -\frac{\partial\psi_i}{\partial y}; \qquad v_i = \frac{\partial\psi_i}{\partial x}. \tag{5}$$

All fields are routinely transformed from the layer-wise fields into the vertical barotropic and baroclinic modes, as common in geophysical fluid dynamics.

The forcing in the governing equations is introduced through an imposed, vertically sheared, baroclinically unstable background flow, given by the following streamfunction and added via simple transformation:

$$\Psi_i = -U_i\, y; \qquad \psi_i \longrightarrow \Psi_i + \psi_i, \tag{6}$$

where U_i are the background zonal-velocity parameters of the problem. The resulting governing equations ([20] Phillips 1954) are:

$$\frac{\partial q_1}{\partial t} + J(\psi_1, q_1) + [\beta + S_1(U_1 - U_2)]\frac{\partial\psi_1}{\partial x} = \nu\nabla^4\psi_1 - U_1\frac{\partial q_1}{\partial x}, \tag{7}$$

$$\frac{\partial q_2}{\partial t} + J(\psi_2, q_2) + [\beta - S_2(U_1 - U_2)]\frac{\partial\psi_2}{\partial x} = \nu\nabla^4\psi_2 - U_2\frac{\partial q_2}{\partial x} - \gamma\nabla^2\psi_2, \tag{8}$$

where advection of the PV anomalies by the background flow can be interpreted as the external forcing.

The main parameters of the above model are the following. The basin size is $L = 1500$ km, which is a compromise between our desire to keep the computational domain as small as possible and, thus, avoid unnecessary computational costs, and the other desire to have the domain large enough, in order to contain all parts of the vortex solution and to avoid the doubly periodic domain interferences. The layer depths are $H_1 = 1$ km and $H_2 = 3$ km, which translates into the stratification parameters S_1 and S_2 being such, that the first Rossby deformation radius of the model is $Rd_1 = 25$ km, hence, the domain size is 60×60 Rd_1. The midlatitude planetary vorticity gradient is $\beta = 2\times10^{-11}$ m^{-1} s^{-1}. The employed reference eddy viscosity value is $\nu = 10$ m^2 s^{-1}; and $\gamma = 4\times10^{-8}$ s^{-1} is the reference bottom friction value, which corresponds to 290 days of spin-down time (note: both ν and γ are varied in Section 4). The Reynolds number based on Rd_1, as well as on the reference ν and typical velocity $U = 0.1$ m s^{-1} is $Re = U\,Rd_1/\nu \approx 250$, which indicates the strongly nonlinear nature of the flow regimes.

For simplicity, we assume $U_2 = 0$ and look for statistically equilibrated turbulent regimes in unstable WB flows with negative upper-layer PV gradient, $\beta + S_1U_1 < 0$, because they tend to support coherent vortices rather than intense alternating zonal jets, as common in unstable EB flows with the positive PV gradient, $\beta + S_1U_1 > \beta$ (e.g., see [22] Berloff et al. 2011). This implies that we consider negative *supercritical* values of U_1, ranging from $2U_C$ to U_C, where $U_C = -\beta/S_1 = -1.8$ cm s^{-1} is (approximately) the critical velocity, at which the WB flow becomes baroclinically unstable. For the subcritical values $U_C < U_1 < 0$, we unsurprisingly found that initialized intense vortices eventually die out (note: this is also true for EB flows).

Our numerical model employs the second-order finite differences, high-accuracy CABARET advection scheme ([33] Karabasov et al. 2009) and direct elliptic solver. Convergence studies and high-Reynolds-number solutions with this type of model are discussed elsewhere ([34] Shevchenko and Berloff 2015). The model equations with the doubly periodic boundary conditions and mass conservation constraint are solved numerically on 512^2 grid, that is, with about 3 km nominal resolution. This resolution provides 8.5 grid intervals for Rd_1, which is decently eddy-resolving category for our high-accuracy advection algorithm. We also checked that spatial resolution is consistent with the viscosity value, in the sense that solutions are indeed numerically converged, on qualitative level. In particular, we checked that doubling grid resolution to 1024^2 nodes results in qualitatively similar reference solutions: for example, for the "strong" reference regime (Section 3), which is more sensitive to spatial resolution, the peak of PV anomaly becomes 5% stronger and propagates 7% faster in the zonal direction. Next grid doubling yielded only a few percents changes. From these experiments we concluded that our numerical resolution is adequate for the reported results.

Statistically equilibrated solutions were computed as an initial-value problem, starting from a state already found for nearby parameter values. The very first "weak" and "strong" solutions were obtained by initializing with weak- and strong-amplitude Gaussian-shape vortex, respectively. The standard deviation of the Gaussian perturbation was $2Rd_1$, and its weak and strong amplitudes were chosen so that the maximum Rossby number was 0.1 and 1, respectively. Since the governing equations (7)–(8) are symmetric with respect to vortex sign parity, we restrict our story only to vortices with positive PV cores in the upper layer. All vortices propagate to the west, but with the above restriction imposed, the resulting vortices also propagate meridionally in the northward direction. Considering the opposite-sign situation is trivial by flipping both the vortex sign and the meridional propagation direction. The spin-up times, which are always found experimentally, are typically such that the vortex crosses about 100 basins (with $L = 1500$ km), and this typically takes more than 100 years. After the spin-up stage, each simulation is saved for further analyses for about 140 years, with the frequency of one record every 10 days, which is enough for our purposes. Note that considering such long-time scales is an idealization, aiming to establish the conceptual ground. This is akin to considering steady-state or circular vortex solutions, which are also idealized objects. All statistically equilibrated model solutions are analyzed and discussed in sections 3 and 4, focusing on the dominant "baroclinic vortex pulsar (BVP)", which we reduce to "vortex pulsar" for brevity. Our definition of any BVP is that this is a pulsating coherent vortex-wave structure, which is persistent on baroclinically unstable background flow.

We consider evolution of vortex pulsars on unstable vertical shears that generate their own growing perturbations, which interact with the pulsar and kick it around. Strong enough perturbations may either break a vortex pulsar or induce alternating zonal jets influencing its evolution. In order to elucidate internal vortex pulsar dynamics, we selected the upper-layer peak PV anomaly as the pulsar center and opted to suppress far-field perturbations by introducing peripheral damping term to the right-hand sides of (7) and (8): $-\delta q_i$, which acts only beyond $10Rd_1$ radius of the circle, centered on the vortex considered. The vortex pulsar itself, up to the far-field circle surrounding its core, remains intact from this damping. We chose the reference value $\delta = 10^{-7}$ s^{-1}, which is inverse of the spin-down time of 116 days, but varied it in Section 4. In other words, a circle around the vortex with the diameter equal to 1/3 of the domain is excluded from any damping, but the flow perturbations in the remaining part of the domain are weakly damped.

3. Main results

Let us start the discussion of results by showing and analyzing two distinctly different vortex pulsars obtained for exactly the same set of parameters (by starting from different initial conditions; see Section 2); their snapshots are in Figs. 1 and 2. Both flow patterns have significant asymmetry, that is, deviations from a circular symmetric

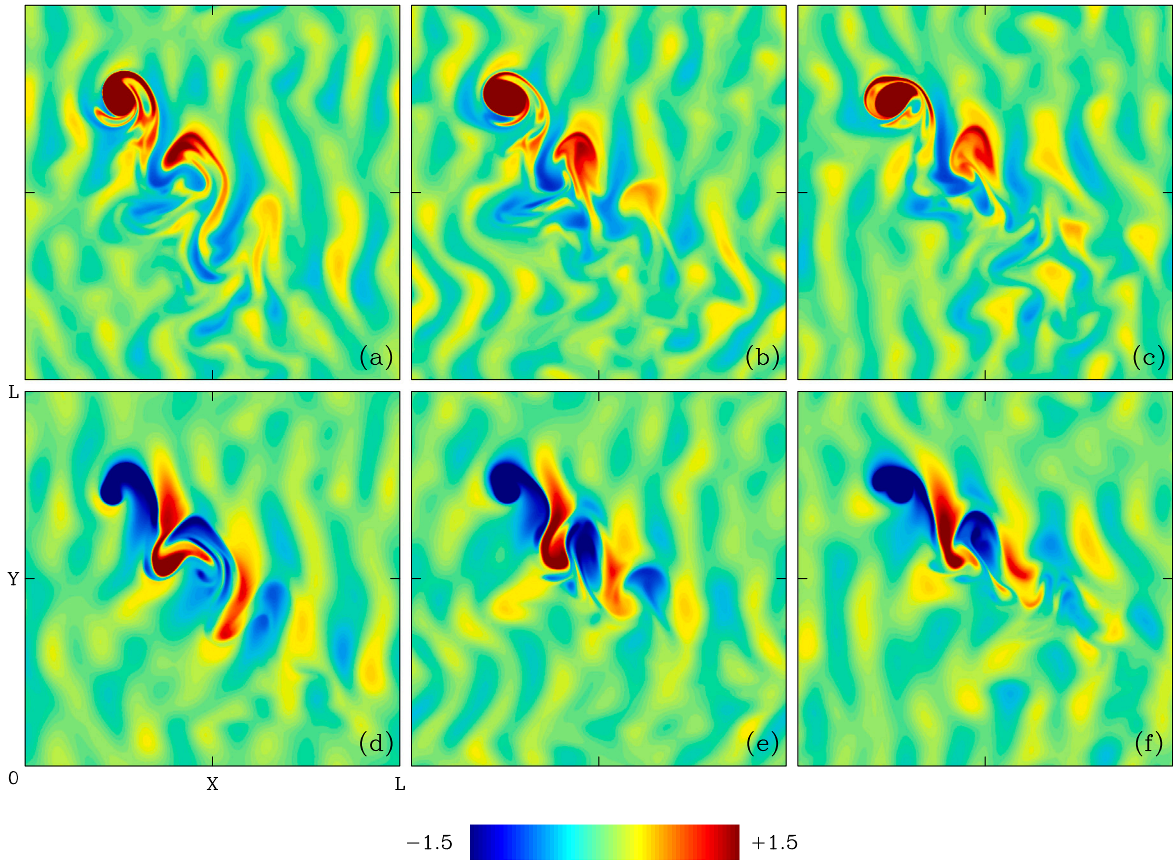

Fig. 1. Typical strong vortex pulsar for $U_1 = -3$ cm s^{-1} and reference parameters. Shown is statistically equilibrated flow state in the full domain, hence there are also weak flow perturbations surrounding the strong pulsar; all the other similar flow illustrations further below also show full domain and statistically equilibrated flow states. Upper/lower panels show upper-/deep-ocean instantaneous snapshots of PV anomaly separated by 100 days; each column of two panels is one snapshot. Since the domain is doubly periodic, it is positioned so that maximum of the upper-ocean PV anomaly is located at $(x, y) = (L/4, 3L/4)$. This set-up masks propagating nature of the vortex and essentially shows it in the co-propagating reference frame. The PV anomaly fields are shown in nondimensional units, with the length scale being grid interval 2.93 km and the velocity scale being 0.01 m s^{-1}. Note the compact, rapidly rotating PV core and the Rossby wave wake trailing to the south-east. Ambient flow field displays supercritical perturbations, which are being damped out.

state, and evolve in time. The former pattern is more energetic, less wavy in the trailing wake, has more intense vortex core and propagates meridionally (to the north) at a steeper angle (away from the westward direction). We refer to the dominant parts of these solutions as "strong" and "weak" baroclinic vortex pulsar (BVPs), respectively, and the corresponding meanings will be explained below in due course.

Time series of the most important vortex pulsar properties are shown in Figs. 3 and 4, to illustrate their statistical equilibration, temporal variability and overall robustness. The strong pulsar is more energetic, due to the intense core that contains most of the relative vorticity and PV anomaly; this is also confirmed by an order larger values of the maximum Rossby number. Note, that large Rossby number of about 0.4 indicates that the QG model operates beyond its formal asymptotic limit and suggests future extension of our study into the primitive equations.

In each vortex pulsar we found position of the peak PV anomaly value in the upper layer (recall that we consider only cyclonic vortices), and used it for shifting the whole coordinate system with the origin placed in this position (the pulsar center). Evolution of the center in time is the vortex trajectory, and it turns out that these trajectories are nearly straight lines, and propagation velocity $\mathbf{c}(t)$ along each trajectory is nearly constant. Each cyclonic vortex pulsar propagates in the north-westward direction, but the strong type propagates at a steeper angle, which is also indirectly pointed out by the trailing wake orientation in the co-moving frame of reference (Fig. 1). Some BVPs, especially of the weak type and for small U_1, have significant variability of the trajectory; in such cases we fitted in a straight line and considered it as the mean-state trajectory.

In the coordinate system steadily moving with the mean propagation velocity $\mathbf{c}=(c_x, c_y)$, we transformed the coordinates as $\mathbf{x} = \mathbf{x}_{old} - \mathbf{c}t$, and this allowed us to rewrite Eqs. (7) and (8) as:

$$\frac{\partial q_1}{\partial t} - c_x \frac{\partial q_1}{\partial x} - c_y \frac{\partial q_1}{\partial y} + J(\psi_1, q_1) + \frac{\partial \psi_1}{\partial x}\,[\beta + S_1 U_1] + U_1 \frac{\partial q_1}{\partial x} = \nu \nabla^4 \psi_1\,,$$
$$\frac{\partial q_2}{\partial t} - c_x \frac{\partial q_2}{\partial x} - c_y \frac{\partial q_2}{\partial y} + J(\psi_2, q_2) + \frac{\partial \psi_2}{\partial x}\,[\beta - S_2 U_1] = \nu \nabla^4 \psi_2 - \gamma \nabla^2 \psi_2\,.$$

In the co-moving coordinate system attached to the BVP center, the surrounding fluid moves around the PV core in the upper layer and passes through the wake in both layers, qualitatively similar to the analytical prediction for the marginally stable shear ([25] Sutyrin et al. 2021a). The dominant pattern of wake is negative PV anomaly in the lower layer, which is offset to the north-east relative to the vortex pulsar center. This pattern is responsible for the positive energy input $E_{input} = -U_1 F_{PV}$ from the available potential energy of the background flow, where the meridional PV flux, $F_{PV} = -H_1 \langle q_1 \partial \psi_1 / \partial x \rangle$ defines the meridional heat flux playing the key role in the eddy feedback to the mean flows (and climate variability). It is defined by both zonally

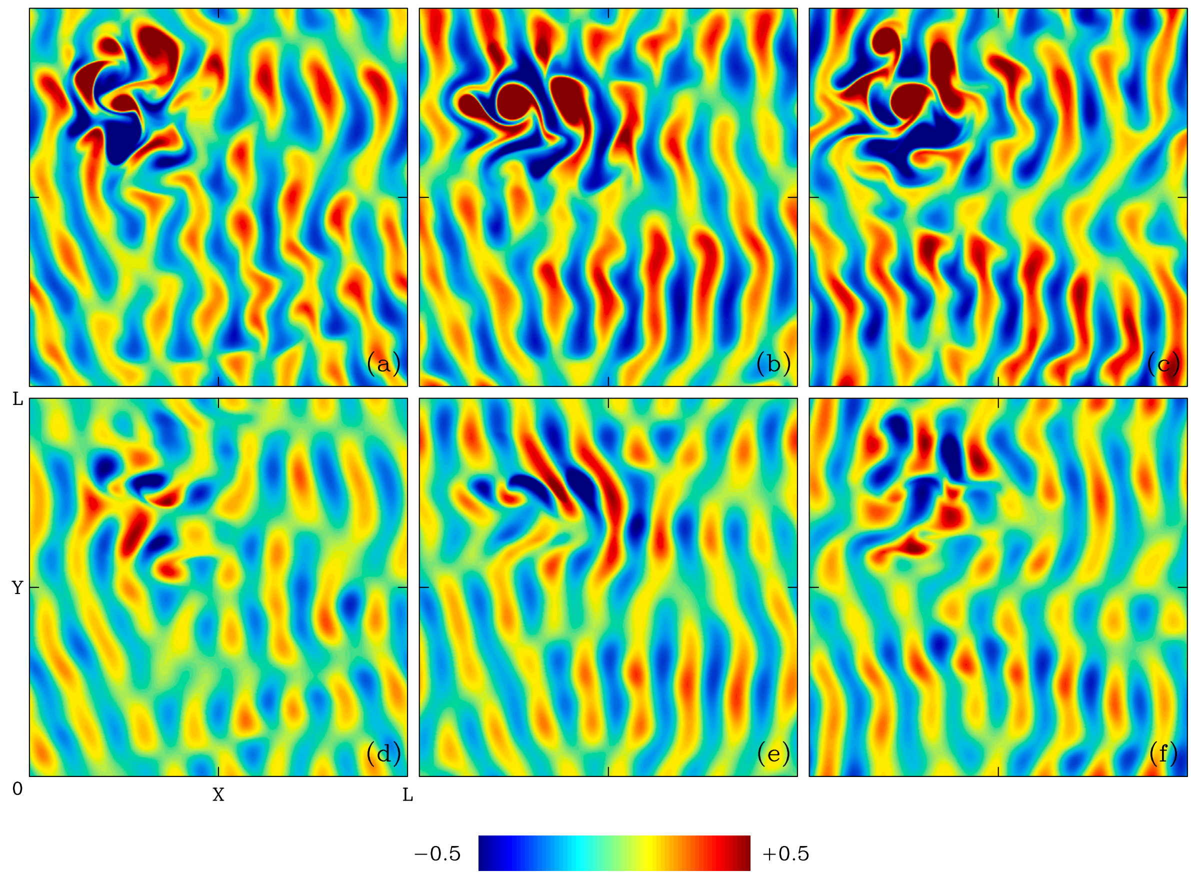

Fig. 2. Same as Fig. 1 but for the weak pulsar (for the same $U_1 = -3$ cm s^{-1} and the other reference parameters). The flow pattern is more wavy and weaker than that of the strong pulsar.

symmetric and zonally asymmetric parts of the upper-ocean flow related to the wake and induced by both zonal, c_x, and meridional, c_y, propagation velocity components of the PV core ([10] Sutyrin 2023).

Let us look closer at the deep-ocean pattern, which significantly differently in the strong and weak pulsars. The position of the corresponding PV anomaly minimum was used as the working definition of the horizontal difference between the dominant PV anomaly patterns in the lower and upper layers. The corresponding difference between the positions is referred further as the combination of the zonal and meridional "tilts", respectively (see Figs. 3c,e and 4c,e). Since the vertical model resolution has only 2 layers, the vertical tilt is completely described by the two distances. The weak pulsars are significantly more tilted than the strong ones, but all of them have noticeable and persistent tilts larger than Rd_1. Both tilt components are negative, which is consistent with the lower-layer PV anomaly being (relative to the upper-layer core) offset north-eastward, in accord with the north-westward vortex pulsar translation. Note, that in the weak pulsar, the lower-layer negative PV anomaly core is sometimes not clearly distinct from the other negative PV anomalies in the wake — this explains occasionally very large tilt values.

Now, let us consider the time-mean fields of the strong reference pulsar illustrated by Fig. 1 and characterized by the considered time series (Fig. 3). The PV anomaly patterns are dominated by horizontally offset, intense cores — positive/negative in the upper-/deep-ocean — accompanied by the wake (Fig. 5). The wake is seen better in the streamfunction pattern, and it is south-eastward of the cores, which is opposite to the direction of the pulsar propagation, and is more pronounced in the deep ocean. It is characterized by several periods and overall decay of the amplitude away from the core. Note, that we could not reduce the model domain size further, because this would start damaging the wake by its interference with the doubly periodic neighbors.

For further analysis we present the time-mean strong reference pulsar in terms of the barotropic and baroclinic vertical modes (Fig. 6). Note, that in the presence of the background shear these standard modes are not the dynamical normal modes ([35] Berloff and Kamenkovich 2013), but the corresponding normal mode analysis and projection on the dynamical modes are deferred for the future. The barotropic-mode core is relatively small and shielded, in the sense that it is surrounded by negative ring of PV anomaly; the baroclinic-mode core is twice as large across and is not shielded. The wake can be seen in both vertical modes, but the baroclinic one decays at the smaller spatial scale, thus, leaving the far field more barotropic.

We checked also to what degree the vortex is depth-compensated, that is, with vanishing small deep-ocean flow; this property can be interpreted as enhanced BVP isolation (or localization) in the vertical direction. Increased depth compensation makes pulsars less sensitive to bottom friction and, most likely, to topographic bottom effects. In the two-layer setting, full depth compensation corresponds to complete correlation (of unity value) between the vertical modes. Here, we found the correlation coefficient of 0.44, suggesting that the strong pulsars are indeed significantly depth-compensated.

We continue our analysis along the following line aiming to comprehend the pulsar asymmetries. It is natural to decompose the flow pattern into its circular symmetric core and the residual asymmetric part, characterizing the wake, as these are qualitatively the dominant

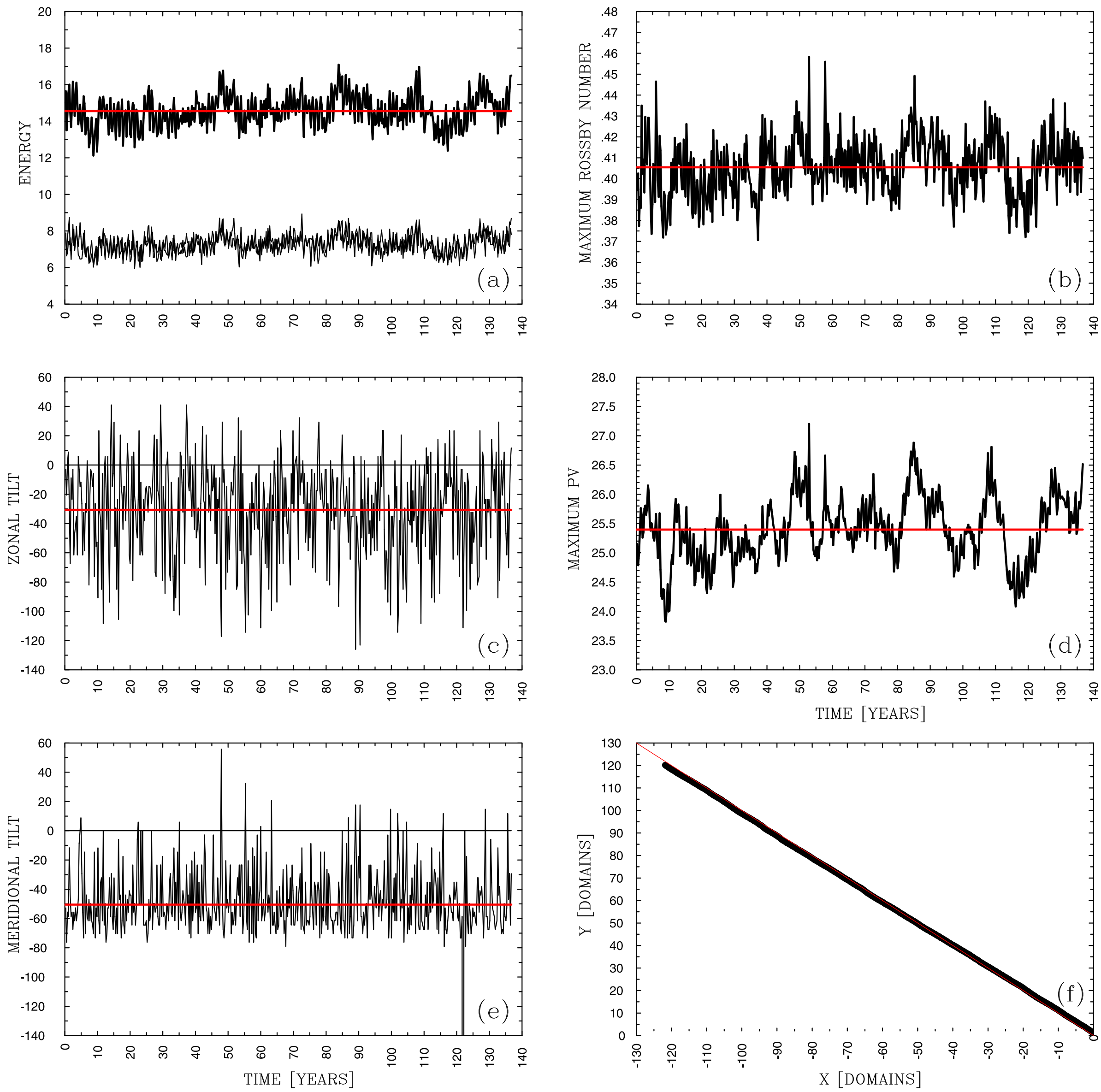

Fig. 3. Time series of the strong pulsar shown in Fig. 1. (a) Total energy (upper curve) and its kinetic energy component (lower curve), all in nondimensional units; energy fluctuations are ±20% around the mean value; kinetic energy is about half of the total energy and the other half is available potential (thermal) energy. (b) Maximum Rossby number, which is found as the maximum ratio of the relative vorticity $\nabla^2\psi_1$ to the planetary vorticity $f_0 = 10^{-4}$ s^{-1}; its time-mean value is about 0.4. (d) Maximum PV value, which is noticeably correlated with the maximum Rossby number but less noisy; compare with (b). (c) and (e) show zonal and meridional (vertical) tilts, respectively, both in kilometers; recall that $Rd_1 = 25$ km; horizontal black lines indicate zero values. (f) Trajectory of the vortex center is shown by thick black curve; propagation is nearly steady. Red lines indicates time-mean values of the corresponding curve, except for panel (f), where it indicates $\pi/4$ angle for the direction of propagation (relative to the westward direction and clockwise).

pulsar components. We recall here that even weak wake has fundamental effect on the vortex dipoles, because it breaks the symmetry and enables the key dynamical mechanisms ([32] Davies et al. 2024); therefore, understanding the wake is important. We imposed azimuthal averaging within the circle centered on the pulsar core of the corresponding layer and having the diameter of $L/2$. This procedure was applied separately to the q and ψ fields, because it does not commute with the elliptic PV inversion (3)–(4). The outcome (Fig. 7) of this decomposition shows that the upper-ocean wake is attached to the core via PV anomalies corresponding to a small offset in the north-eastward direction. In other words, the asymmetric wake is accompanied by certain asymmetry of the core itself. On the vortex pulsar core, the residual streamfunction is dominated by a dipolar circulation with northward orientation, which corresponds to ventilation of the core in the time-mean sense. In the deep ocean (Fig. 8), the residual wake is more pronounced and forms an integral part of the core itself, by shifting it south-eastward.

Next, let us consider the time-mean fields of the weak reference pulsar, as illustrated by Fig. 2. To shorten discussion of the undertaken analyses, we show only the vertical modes of the pulsar decomposition (Fig. 9). The baroclinic mode is stronger than the barotropic one; the barotropic core is not shielded, as in the strong pulsar, and the barotropic streamfunction anomalies cover zonally the whole domain. This implies that the weak pulsars have relatively more active far-field barotropic velocity and, therefore, will have more significant vortex-vortex interactions, when considered as vortex gas ensembles. It is

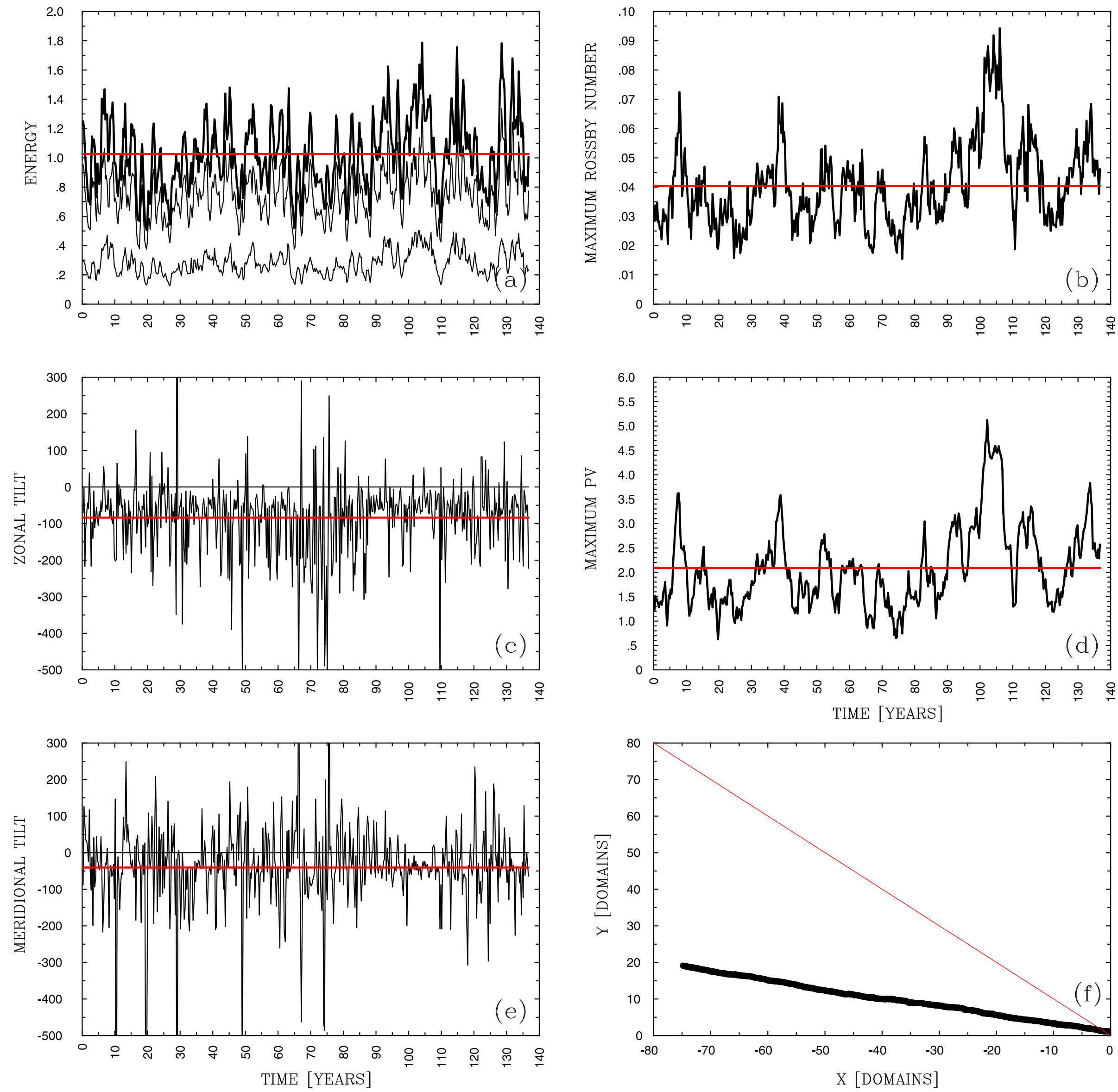

Fig. 4. Time series for the weak pulsar shown in Fig. 2. Same figure set-up as in Fig. 3. (a) Notice much smaller energy values and a lot more pronounced potential energy contribution. (b) Notice that Rossby number is by order of magnitude smaller than for the strong pulsar. (c) and (e): notice much larger tilt values and its variability. (f) Notice much slower propagation and smaller angle of propagation.

not even possible to say that the wake is to the east of the vortex, as it clearly penetrates westward, even in terms of the baroclinic PV anomalies. Because of the long-range components, the weak pulsars are expected to interact more efficiently with the other vortices and basin boundaries. We found that the vertical-mode correlation is 0.17, which suggests relatively weak depth compensation (compared to the strong pulsar), therefore, weak pulsars are less localized both horizontally and vertically, and because of the latter should be more sensitive to bottom friction and topography.

Local Okubo-Weiss parameter $W(t,x,y)$ is a measure of the relative importance of deformation and rotation at a given point and is widely used for identifying and describing oceanic vortices. It is defined (omitting layer index) as the following:

$$S_n = \frac{\partial u}{\partial x} - \frac{\partial v}{\partial y} = -2\frac{\partial^2 \psi}{\partial x \partial y}\,, \qquad S_s = \frac{\partial v}{\partial x} + \frac{\partial u}{\partial y} = \frac{\partial^2 \psi}{\partial x^2} - \frac{\partial^2 \psi}{\partial y^2}\,,$$
$$W = S_n^2 + S_s^2 - \zeta^2\,,$$

where S_n and S_s are the normal and shear strains, respectively, and $\zeta = \nabla^2\psi$ is relative vorticity. For brevity, we do not present maps of Okubo-Weiss parameter; they all show large negative values in the vortex cores, which are surrounded by narrow rings of small positive values. This indicates fundamental difference between the core and periphery, as typical for coherent vortices ([3] McWilliams 1984). For the strong pulsars, $W(t,x,y)$ fields have negative spatial integrals in both layers and are typically larger in the upper over the deep layer by an order of magnitude. For the weak pulsars, the magnitude of $W(t,x,y)$ is only about 4 times larger in the upper over the lower layer, which is consistent with the less pronounced core of PV anomaly.

Let us now implement the Reynolds decomposition of the vortex pulsars in time and consider the resulting balances in the time-averaged governing equations. Given the standard decomposition into the time mean (indicated by overbars) and fluctuations (indicated by primes),

$$q_i(t,x,y) = \overline{q_i(x,y)} + q_i'(t,x,y)\,, \qquad \psi_i(t,x,y) = \overline{\psi_i(x,y)} + \psi_i'(t,x,y)\,,$$

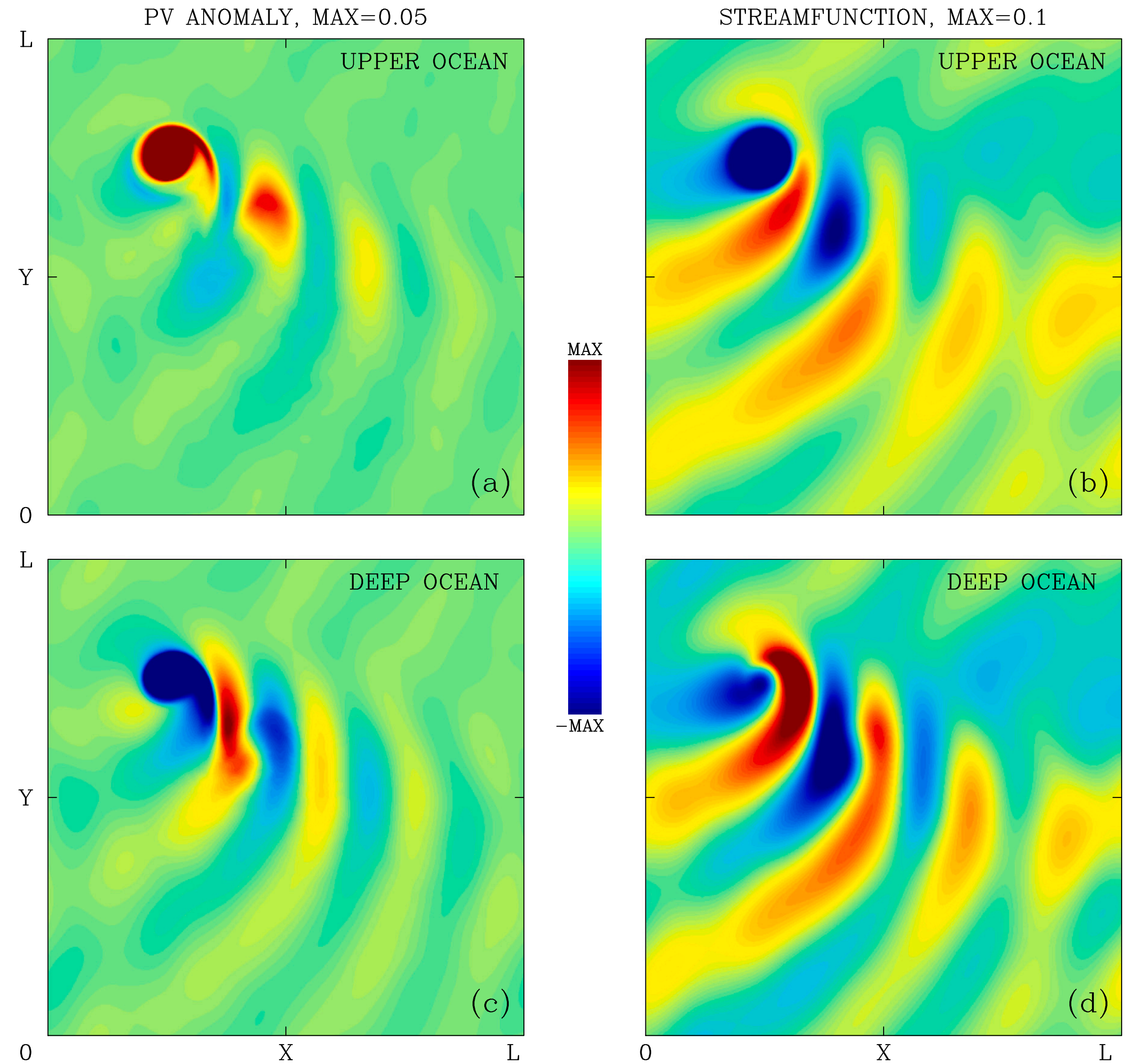

Fig. 5. Time-mean strong pulsar ($U_1 = -3$ cm s^{-1}). Upper/lower panels show upper-/deep-ocean fields; left/right panels show PV anomaly q_i and streamfunction ψ_i, respectively. The center of the upper-ocean PV anomaly is positioned at $(x, y) = (L/4, 3L/4)$, and the domain is doubly periodic. The deep-ocean (negative) PV anomaly is offset with respect to the pulsar center $(x, y) = (L/4, 3L/4)$ by about 30 km to the east and about 50 km to the north, but this is less than 4% of the basin size and, therefore, is hard to see on the plot. The PV anomaly fields are normalized so, that the maximum value of q_1 is unity; similarly, the minimum value of ψ_1 is normalized to be negative unity. Color scale limits for the left and right panels are indicated at the top; colors are oversaturated in order to show better the wake.

we substitute it into the governing equations and take the time averages, assuming that the time-mean of a fluctuation component is zero:

$$J(\overline{\psi_1},\overline{q_1}) - c_x \frac{\partial \overline{q_1}}{\partial x} - c_y \frac{\partial \overline{q_1}}{\partial y} + \overline{J(\psi_1', q_1')} + \frac{\partial \overline{\psi_1}}{\partial x}\left[\beta + S_1 U_1\right] + U_1 \frac{\partial \overline{q_1}}{\partial x} = \nu \nabla^4 \overline{\psi_1},$$
$$J(\overline{\psi_2},\overline{q_2}) - c_x \frac{\partial \overline{q_2}}{\partial x} - c_y \frac{\partial \overline{q_2}}{\partial y} + \overline{J(\psi_2', q_2')} + \frac{\partial \overline{\psi_2}}{\partial x}\left[\beta - S_2 U_1\right] = \nu \nabla^4 \overline{\psi_2} - \gamma \nabla^2 \overline{\psi_2}.$$

The involved terms have clear physical interpretations: the first Jacobian is advection of the mean PV anomaly by the mean flow, that is, the mean advection; the following pair of terms describes the tendency term corresponding to the vortex pulsar propagation; the second Jacobian, referred to as the eddy forcing, describes advection of the fluctuation PV anomaly by the flow fluctuations; and this is followed by the meridional advection of the background PV by the mean flow (in both layers) and the zonal advection of the mean PV anomaly by the background flow (in the upper layer only). The viscous and frictional terms, which we deliberately kept on the right-hand side were found relatively small. The nonlinear (minus) eddy forcing term can be further split into the Reynolds and form stress components,

$$\overline{J(\psi_1', q_1')} = \overline{J(\psi_1', \zeta_1')} + \overline{J(\psi_1', -S_1(\psi_1' - \psi_2'))},$$
$$\overline{J(\psi_2', q_2')} = \overline{J(\psi_2', \zeta_2')} + \overline{J(\psi_2', -S_2(\psi_2' - \psi_1'))},$$

respectively, where the Reynolds stress describes rearrangement of relative vorticity (and momentum) by the vortex fluctuations, and the form stress describes the rearrangement of layer thickness (and buoyancy or heat). Note, that the form stress terms have some cancellation inside, because the flow does not interact nonlinearly with itself, but we retain this formulation for clarity. Similarly, we split the mean-flow advection into the mean-flow Reynolds and form stresses (not shown), which are also referred to as the mean-flow relative-vorticity and heat advection.

We continue analysis of the pulsars by considering the time-mean dynamical balances (in the co-moving coordinate system) of the reference solutions. The main upper-ocean balance of the strong pulsar is between the mean-flow advection, tendency and PV advection by the background flow (Fig. 10), and it dominates the vortex core. The mean-flow advection is dominated by the heat component, although

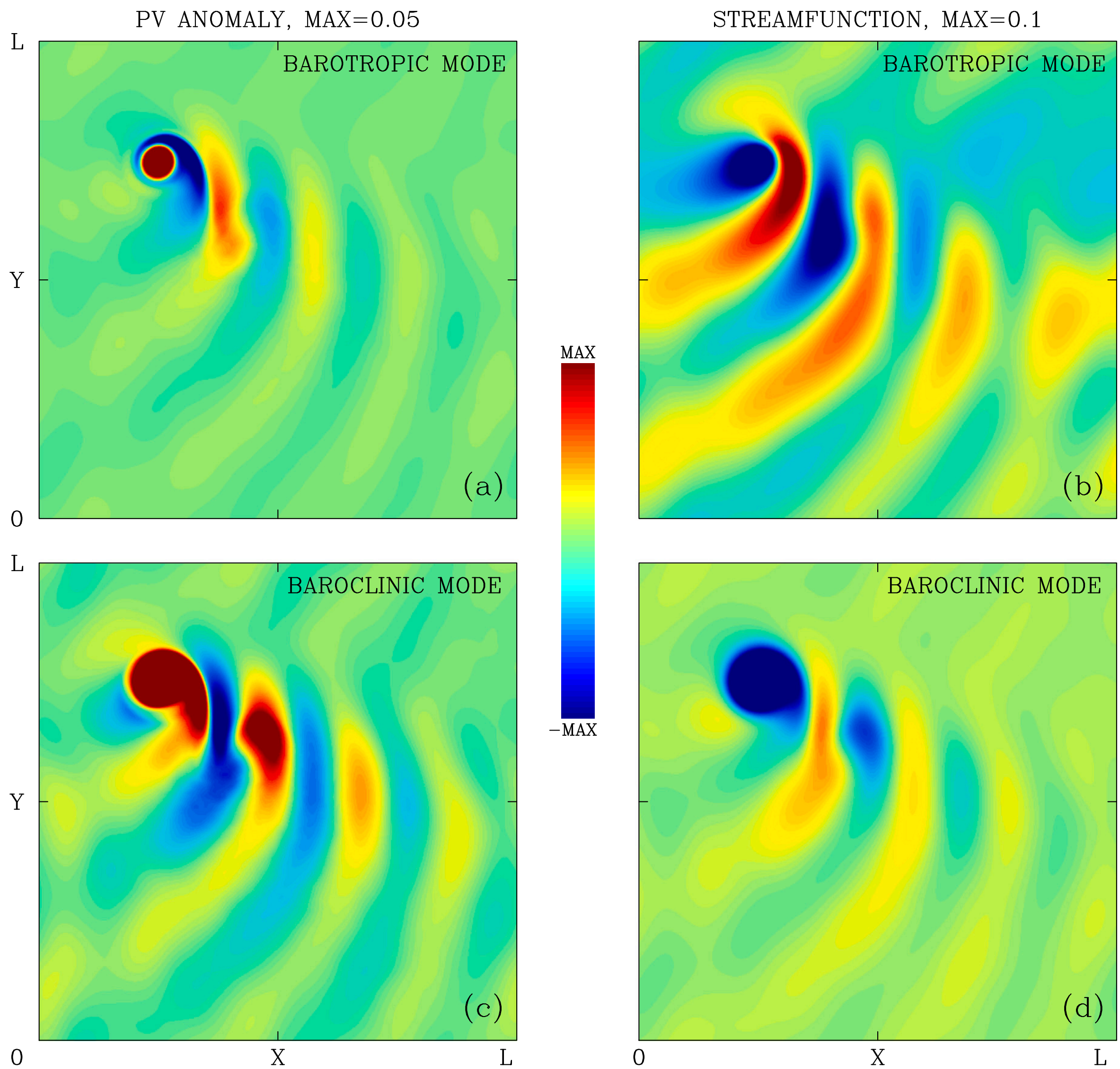

Fig. 6. The same set-up as in Fig. 5, but for the vertical modes rather than layers. Upper/lower panels show barotropic/baroclinic time-mean fields; left/right panels show PV anomalies and streamfunctions, respectively.

relative-vorticity component is significant — this implies that the main large-scale effect of the strong pulsars will be thermodynamical. The eddy forcing and advection of background PV are relatively small but significant, whereas the diffusion term is very small and insignificant (not shown). The eddy forcing term becomes significant and enters the main balance only for the largest shears ($U_1 < -3.5$ cm s^{-1}), and this change of balance corresponds to the observed increase of the meridional and decrease of the zonal propagation (Section 4). This is an important observation, as it indicates that we have not yet reached the most turbulent effects, and these effects are clearly well beyond the QG asymptotics; the very low-viscosity extension of our study needs to be carried out in dynamically more comprehensive primitive equations. In the deep ocean the main dynamical balance (Fig. 11) extends beyond the core, into the wake, and it is between the mean-flow advection, which has equally important Reynolds and form stresses, and the tendency term. Advection of the background PV is relatively small but significant in the wake, whereas the eddy forcing (shown), as well as the diffusion and bottom friction terms (not shown) are all insignificant.

The dynamical balance for weak reference pulsar (Figs. 12 and 13) is quite different from one for the strong pulsar. The main upper-ocean dynamical balance is between the tendency and PV advection by the background flow, which implies that the pulsar tends to propagate slower than the background flow; in other words, it tends to propagate against it. Both the mean-flow advection, which is completely dominated by the form stress, and meridional advection of the background PV are relatively small but still significant. By the set-up, in the deep ocean there is no background flow, therefore, the main balance is between the tendency term and advection of the background PV, and this balance dominates the wake rather than the pulsar core. Thus, we report that in both types of pulsars, the deep-ocean balance fundamentally involves the wake, hence, it involves the pulsar asymmetry.

Next, we show flow perturbations, typical for strong pulsars (Fig. 14), that were obtained by subtracting the corresponding time-mean pattern (Fig. 5) from the full flow snapshots (Fig. 1). Perturbation fields clearly exhibit co-rotating, baroclinic quadrupole mode on the pulsar core. This mode corresponds to rotating elliptical deformations,

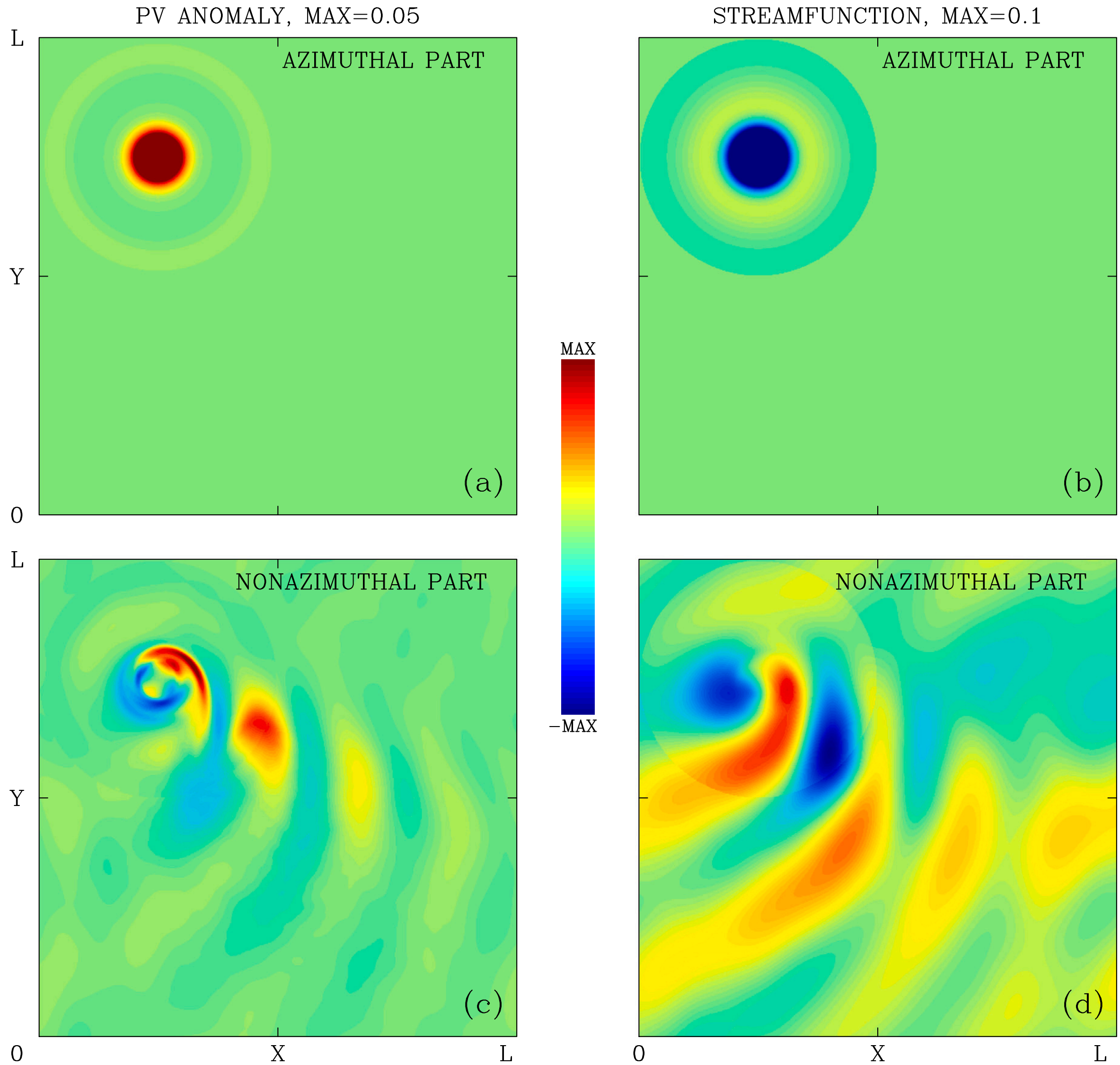

Fig. 7. Circular symmetric and residual decomposition of the strong reference pulsar ($U_1 = -3$ cm s^{-1}). The same set-up as in Fig. 5, but only for the upper ocean. Upper/lower panels show circular/residual components of the time-mean fields; left/right panels show PV anomalies and streamfunctions, respectively. The PV anomaly fields are normalized so, that the maximum value of q_1 is unity; similarly, the minimum value of ψ_1 is negative unity. Color scale limits for the left and right panels are indicated at the top; colors are oversaturated in order to show better the wake.

which stretch the pulsar in one direction but also squeeze it in the transverse direction. This behavior produces PV filaments that are shed away from the pulsar and, thus, remove excessive PV anomaly that accumulates due to the down-gradient meridional propagation of the vortex. Exploration of this process, here referred to as material ventilation of the vortex core, needs detailed Lagrangian analyses, and, therefore, goes beyond the limited scope of this study. We looked at various diagnostics and their temporal spectra (not shown), and the best one for the quadrupole mode is the second moment of the PV anomaly in the BVP core: it naturally picks up the elliptic perturbation and clearly shows that its dominant variability has the time period of 9–10 years. Since this time scale is long, relative to typical oceanic-vortex life time, its extraction from the observed real-ocean data may be not possible, but observing in the data elliptic vortex shapes must be possible (e.g., [9] Chen et al. 2019).

We do not show similarly extracted perturbations for the reference weak pulsar, because the time-mean component is relatively small and does not mask any significant features of the perturbations beyond those seen in the full-flow snapshots (Fig. 2). The temporal spectra of the time series we looked at are also broad-band and noisy, suggesting that variability of the weak pulsar is multi-scale and complicated.

Finally in this section, we consider dependencies of the pulsar characteristics on the peripheral damping parameter δ (Fig. 15). First, by looking at the maximum Ro, we conclude that the reference value $\delta = 10^{-7}$ s^{-1} indicates the critical level of damping, which begins to matter. The lower values of damping have nearly no effect on the vortex pulsar intensity but efficiently iron out perturbations in the far field and prevent them from impacting the BVP. These far-field perturbations are illustrated by Fig. 16, where twins of the reference pulsar are obtained with no damping imposed. Note that a strong pulsar is intense enough to be well-defined in the surrounding sea of much weaker fluctuations, but it is also clear that the fluctuations have noticeable impact on the pulsar itself. In the weak pulsar the surrounding fluctuations are of nearly similar strength, hence, the issues of the weak pulsar recognition and tracking, as well as of vortex-vortex interactions, are all expected to have serious consequences. One of our ancillary conclusions is that with imposed δ-filtering one can study evolution of coherent vortices on rather complicated 3D background flows. However, we recommend use

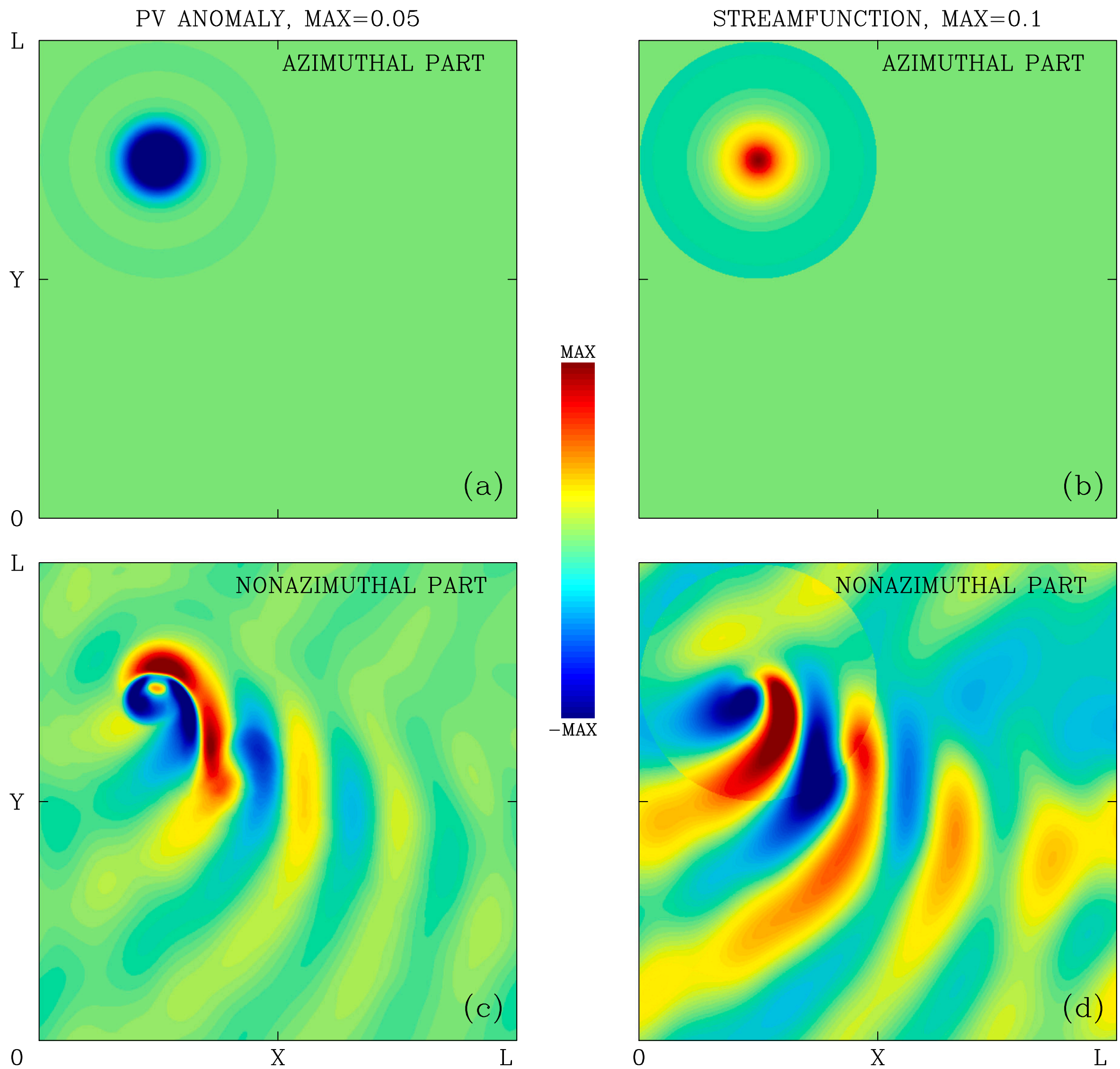

Fig. 8. Circular symmetric and residual decomposition of the reference strong pulsar ($U_1 = -3$ cm s^{-1}). The same set-up as in Fig. 7, but for the deep ocean.

of the peripheral damping intensity not larger than what we used; then, it efficiently controls the level of surrounding turbulence and allows to either isolate or control effects of ambient turbulence on the pulsar characteristics (see Fig. 16).

4. Dependencies on the dissipative parameters and the vertical shear

In the previous section we discussed the reference cases of the strong and weak pulsar for fixed values of the governing parameters: the bottom friction $\gamma_0 = 4 * 10^{-8}$ s^{-1}, the lateral eddy viscosity $\nu_0 = 10$ m^2 s^{-1} and the background velocity $U_1 = -3$ cm s^{-1} corresponding to the supercriticality $\epsilon = U_1/U_c - 1 = 0.67$. In this section we discuss how characteristics of vortex pulsars depend on variations of these parameters.

First, in Fig. 17 we show some dependencies on the normalized bottom friction γ/γ_0 by varying it from zero (no friction) to 40 (spin-down time of about one week). The maximum Rossby number of both pulsar families decreases, while the potential-to-kinetic energy ratio increases monotonically, converging at the largest γ values. Near $\gamma/\gamma_0 \simeq 8$, the zonal propagation speed of the strong BVP becomes less than the background flow speed, while the ratio of the meridional propagation speed to the Rossby number remains nearly the same up to $\gamma/\gamma_0 = 30$, thus, showing persistence of this characteristics. In contrast to the strong BVP, the meridional speed of the weak one decreases with γ much faster than its Rossby number, moreover, the weak BVP propagation becomes pure zonal for $\gamma/\gamma_0 > 10$. The diamonds added to all panels in Fig. 17 correspond to the strongest equilibrated vortex-wave structure analyzed in [26] (Sutyrin et al. 2021b) for the numerical solution to (7)–(8) for $\gamma/\gamma_0 = 15$, $\nu/\nu_0 = 1.2$, and $\epsilon = 1$. Note that statistically equilibrated states in [26,29,30] were always initiated with small random perturbations forming the fastest growing normal modes which become unstable leading to the saturation of vortex properties at the amplitude typical for strong pulsars (compare diamonds and red lines in Fig. 17). Thus, we hypothesize that the strongest vortex was a strong pulsar; dynamical analyses of the vortices emerging in this flow regime remain to be completed in the future.

With fixed $\gamma = \gamma_0$ and varying ν and U_1, we found (Fig. 18) that the BVP characteristics essentially depend on the following combined

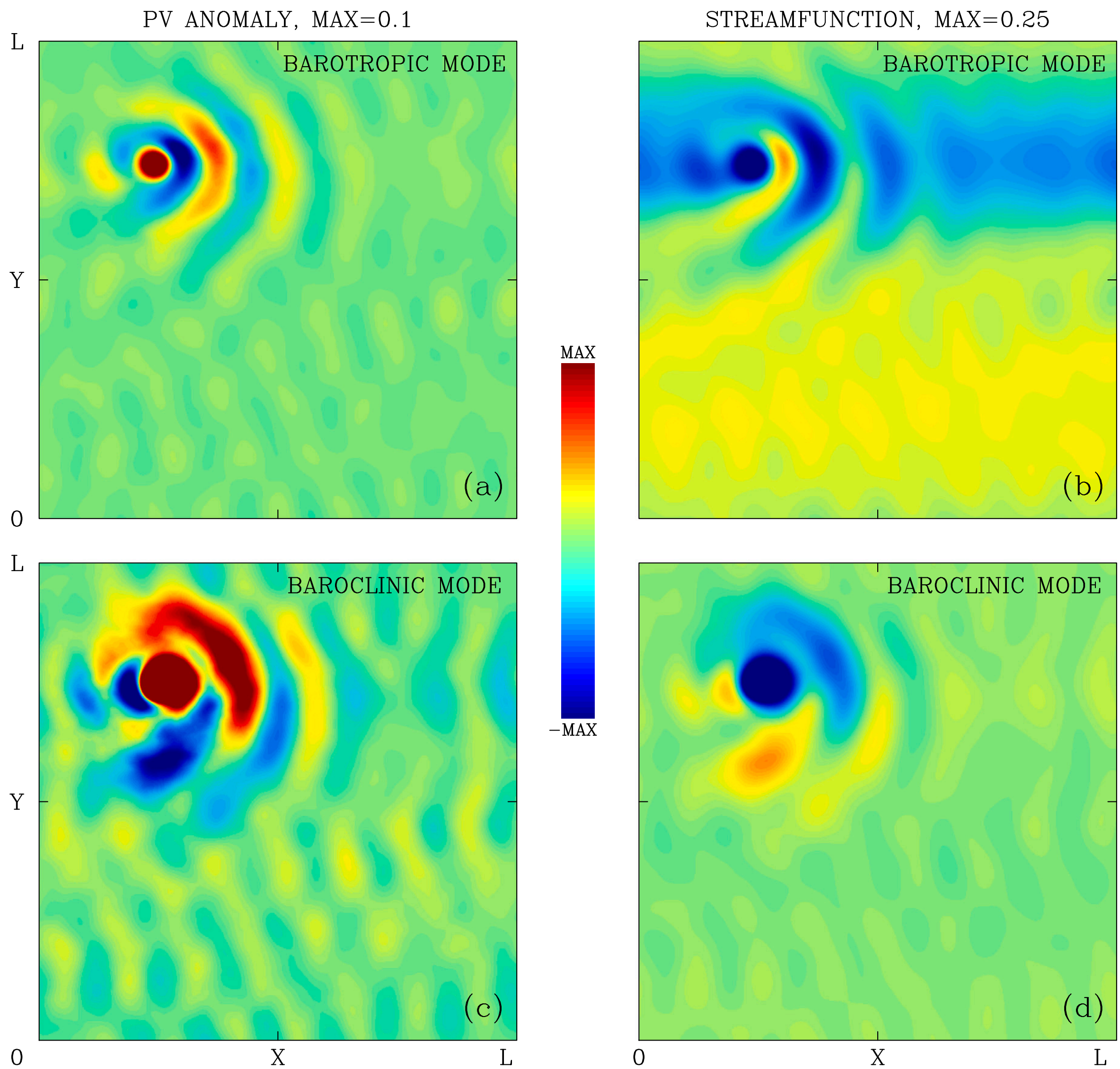

Fig. 9. The reference weak pulsar ($U_1 = -3$ cm s^{-1}). The same set-up as in Fig. 6. We opted to show only modal representation, for the sake of brevity.

parameter:

$$\mu = \frac{(U_1 - U_c)^2 \nu_0}{U_c^2 \nu} = \frac{\nu_0}{\nu}\,\epsilon^2 . \tag{9}$$

Note, that we are limited by finite ν from below, because of the numerical conversion that require doubling the grid nodes for halving the viscosity value ([34] Shevchenko and Berloff 2015); therefore, we varied ν from 2.5 to 200 m^2 s^{-1} ($0.02 < \mu < 1.5$).[2] The supercriticality $(U_1 - U_c)/U_c$ was varied from 0 to 1.22, corresponding to $0 < \mu < 1.5$.

First, for the lower viscosity values or larger supercriticality (increasing μ), intensity of the pulsars increases, but eventually only the strong family survives (Fig. 18). For the BVP intensity, as characterized by maximum Ro, a decrease of ν is nearly equivalent to an increase of the supercriticality squared. Moreover, for the weak pulsars Ro increases with μ nearly linearly: $Ro \sim 0.1\mu$ is found for $\mu < 0.6$. For the strong pulsars $Ro \sim \mu$ is found for $0.3 < \mu < 0.6$, where both families co-exist; $Ro \sim 1.4\mu$ is found for $\mu > 0.6$; and subsequently $Ro/\mu \to 1$ with further increase of $\mu \to 1.5$. Second, ratios of the potential and kinetic energies remain weakly sensitive to μ, as long as $\mu > 0.3$. It increases for the weak pulsars at large ν, due to weakening of the barotropic part of the wake, and it is about 2.5 times larger for the strong pulsars, thus, indicating substantially larger heat anomalies. Third, the zonal velocity component of weak/strong BVP is smaller/larger than the background flow speed for $\mu < 0.8$. The reason for the sharp decrease of the zonal velocity component for the strong pulsars, if supercriticality $\epsilon > 0.9$ (black line) remains to be investigated, but it may be related to the fact that eddy stresses enter the main dynamical balance. Fourth, the zonal velocity components of the pulsars on the two branches are either much faster or slightly slower than the background flow.

Finally, behavior of Ro and the meridional velocity component (Fig. 18a,d) suggests four ranges of μ with distinctly different regimes of weak and strong BVPs, but explanation of the involved physics is deterred until the Lagrangian ventilation mechanics is properly analyzed:

[2] At even lower ν values, the grid needs 1024^2 nodes, hence, we had to leave this for future studies.

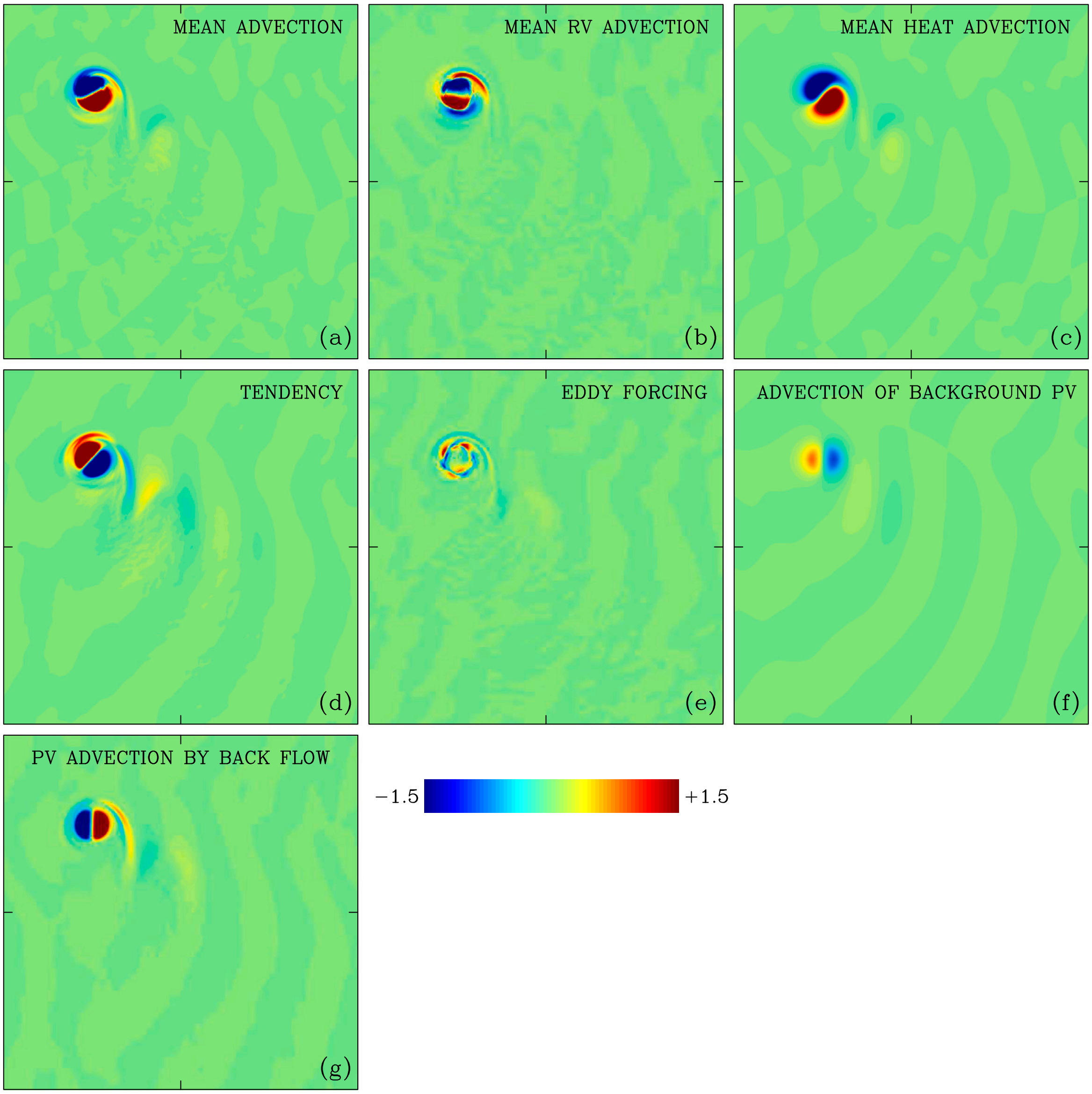

Fig. 10. Individual terms of the time-mean dynamical balance governing the strong pulsar ($U_1 = -3$ cm s^{-1}) in the co-moving coordinate system. (a) Mean advection, $J(\overline{\psi_1}, \overline{q_1})$; (b) mean Reynolds stress, $\overline{J(\psi_1', \zeta_1')}$; (c) mean form stress, $\overline{J(\psi_1', -S_1(\psi_1' - \psi_2'))}$; (d) tendency term, $-c_x \frac{\partial \overline{q_1}}{\partial x} - c_y \frac{\partial \overline{q_1}}{\partial y}$; (e) eddy forcing, $\overline{J(\psi_1', q_1')}$; (f) advection of the background PV, $\frac{\partial \overline{\psi_1}}{\partial x}[\beta + S_1 U_1]$; (g) advection of the mean PV by the background flow, $U_1 \frac{\partial \overline{q_1}}{\partial x}$. The units are nondimensional.

(i) for $\mu < 0.3$, slow meridional velocity component of the weak pulsar increases with μ differently depending on whether ν or ϵ is varied;

(ii) for $0.3 < \mu < 0.6$, the meridional velocity component of the strong pulsar is about 7 times faster than that of the weak pulsars, whether ν or ϵ is varied;

(iii) for $0.6 < \mu < 0.8$, the meridional velocity component decreases sharply (in contrast to further increase of Ro);

(iv) for $0.8 < \mu < 1.5$, increase of the meridional velocity component comes from both ν or ϵ, whereas the zonal velocity component decreases sharply but only due to the increase of ϵ.

We also looked at some other properties of the BVPs, and Fig. 19 shows their tilts (explained in Section 3). The weak-branch tilts imply the distances of about $4Rd_1$ and longer, and the upper-branch tilts — of about $2Rd_1$, and this is mostly due to the difference in zonal distances. The angle of tilt tends to be positive (except for weak shears), which implies that the dominant, deep-ocean negative PV anomaly is offset to the east and to the north of the upper-ocean positive PV anomaly. In general, the weak/strong pulsars have the horizontal tilt directions smaller/larger than $\pi/4$ angle (relative to abscissa direction).

Next, we considered how the energy input $E_{input} = U_1 H_1 \langle q_1 \partial\psi_1/\partial x \rangle$ from the available potential energy of the background flow into pulsar depends on U_1 (Fig. 20a). The main conclusion is that strong pulsar consumes an order-of-magnitude larger intake of the energy, relative to the weak pulsar, and the energy input increases with the background shear. The energy input is nonlocal, because the background flow is supercritical and energy is extracted not only by the vortex pulsar but also by all growing perturbations. Keeping this in mind, we considered the *local* energy input, which is defined as input within the circle of radius $4Rd_1$, centered on the vortex pulsar; we normalized this as the ratio to the total energy input. It turns out that in the strong pulsar about 80% of the energy input is local, whereas in the weak pulsar

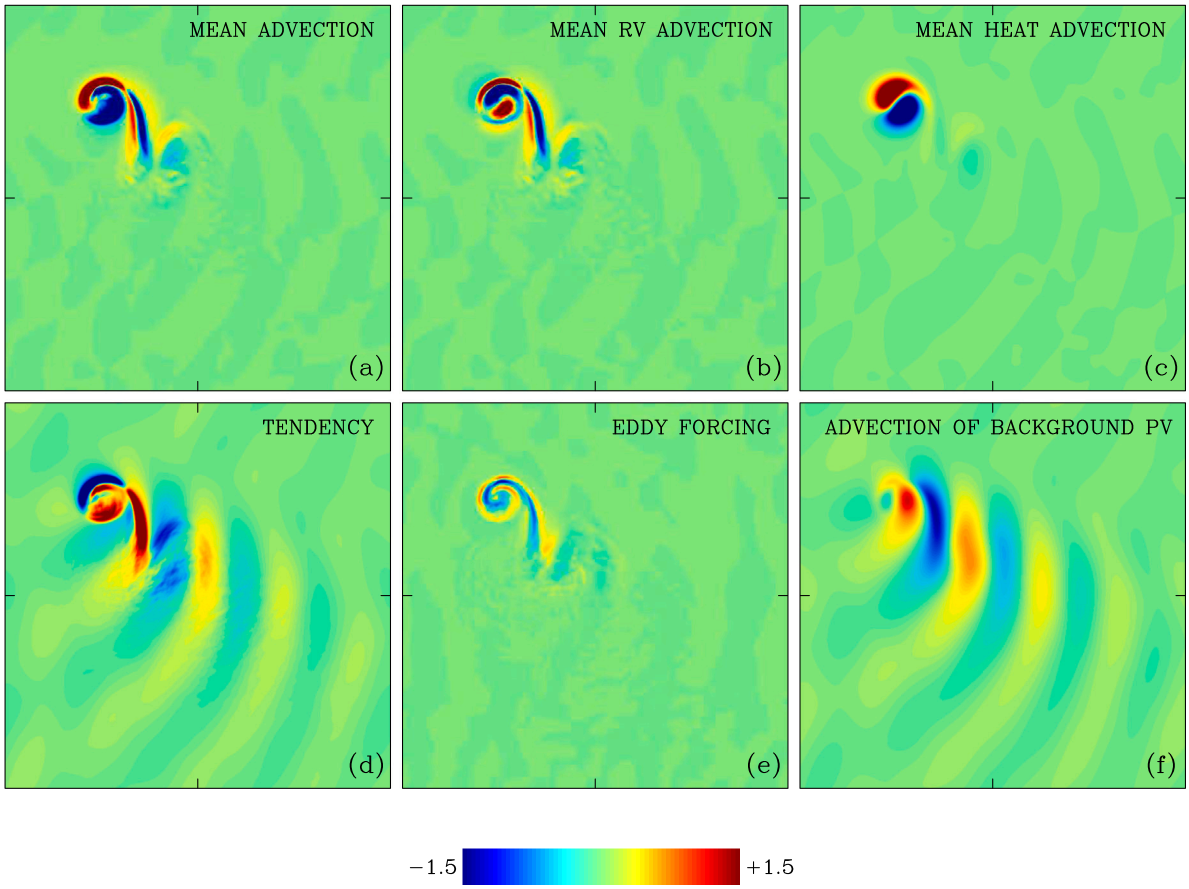

Fig. 11. The same set-up as in Fig. 10, but for the deep ocean. (a) Mean advection, $J(\overline{\psi_2}, \overline{q_2})$; (b) mean Reynolds stress, $\overline{J(\psi_2', \zeta_2')}$; (c) mean form stress, $\overline{J(\psi_2', -S_2(\psi_2' - \psi_1'))}$; (d) tendency term, $-c_x \frac{\partial \overline{q_2}}{\partial x} - c_y \frac{\partial \overline{q_2}}{\partial y}$; (e) eddy forcing, $\overline{J(\psi_2', q_2')}$; (f) advection of the background PV, $\frac{\partial \overline{\psi_1}}{\partial x} [\beta - S_2 U_1]$.

this value drops to only about 10%–20% (Fig. 20b). From this we conclude that the strong family is very efficient and intense, in terms of the energy extraction from the background environment. Finally, we found that fraction of the locally extracted energy that is also locally dissipated is relatively small and less than 20% for all vortex pulsars considered; this fraction also grows from zero linearly with the supercriticality (Fig. 20c). This property is the only one that shows nearly no difference between strong and weak pulsars, where they co-exist for the same parameters. Overall, from this property we conclude that vortex pulsars tend to be open systems, in the sense that they distribute the extracted energy into the surrounding field, where it is eventually dissipated.

An open question remains why does the weak branch disappear or become unstable at large enough U_1 or small enough ν? The first author hypothesizes that this may happen, because the linear normal-mode dispersion curves of linearized dynamics on the top of the background flow become turned around by the background-flow Doppler shift so much (e.g., see Figs. 3 and 5 in [31] Berloff and Kamenkovich (2013)) that the modes having positive group velocity (i.e., those running against the background flow) disappear from the normal-mode spectrum, and this makes it impossible to support the main dynamical balance. The other hypothesis is that the acting normal modes become so unstable (i.e., acquire such strong exponential growth), that the nonlinearity cannot hold the weak pulsar together and it becomes unstable. Further analyses are needed to test both hypotheses, by projecting the weak pulsars on the normal-mode basis (e.g., as in [36] Haigh and Berloff 2020). Why does the strong branch disappear or become unstable at small enough U_1 or large enough ν? The first author hypothesizes that the energy supply from the background pool of available potential energy becomes insufficient for supporting strong pulsar, because of its required high energy consumption for ventilation and balancing out dissipation. This is also consistent with the minimal energy input into the vortex (Fig. 20). Finally, the other hypothesis is the observed disappearance or destabilization of the strong branch for $\mu < 0.3$ could be an artefact of the peripheral damping that suppresses the fastest growing normal mode and thus nonlocally undermines energy supply into the pulsar.

5. Summary and discussion

This study was motivated by the phenomenon of coherent vortices that are ubiquitous in the oceans and atmospheres, because quasi-2D turbulent fluids with strong anisotropy in vertical direction tend to self-organize its relative vorticity in relatively small, rapidly rotating features. These vortices can be viewed as a class of long-lived and spatially localized mesoscale eddies operating on the fundamental length scale of the first Rossby deformation radius Rd_1. There are many motivations to study the oceanic mesoscale eddies, but the main one is their importance in setting up and maintaining oceanic general circulation, which is the main component of the Earth system climate and its variability. The goal of this study is to find robust coherent vortices on simple but unstable background flows, which are common in the oceans and atmospheres.

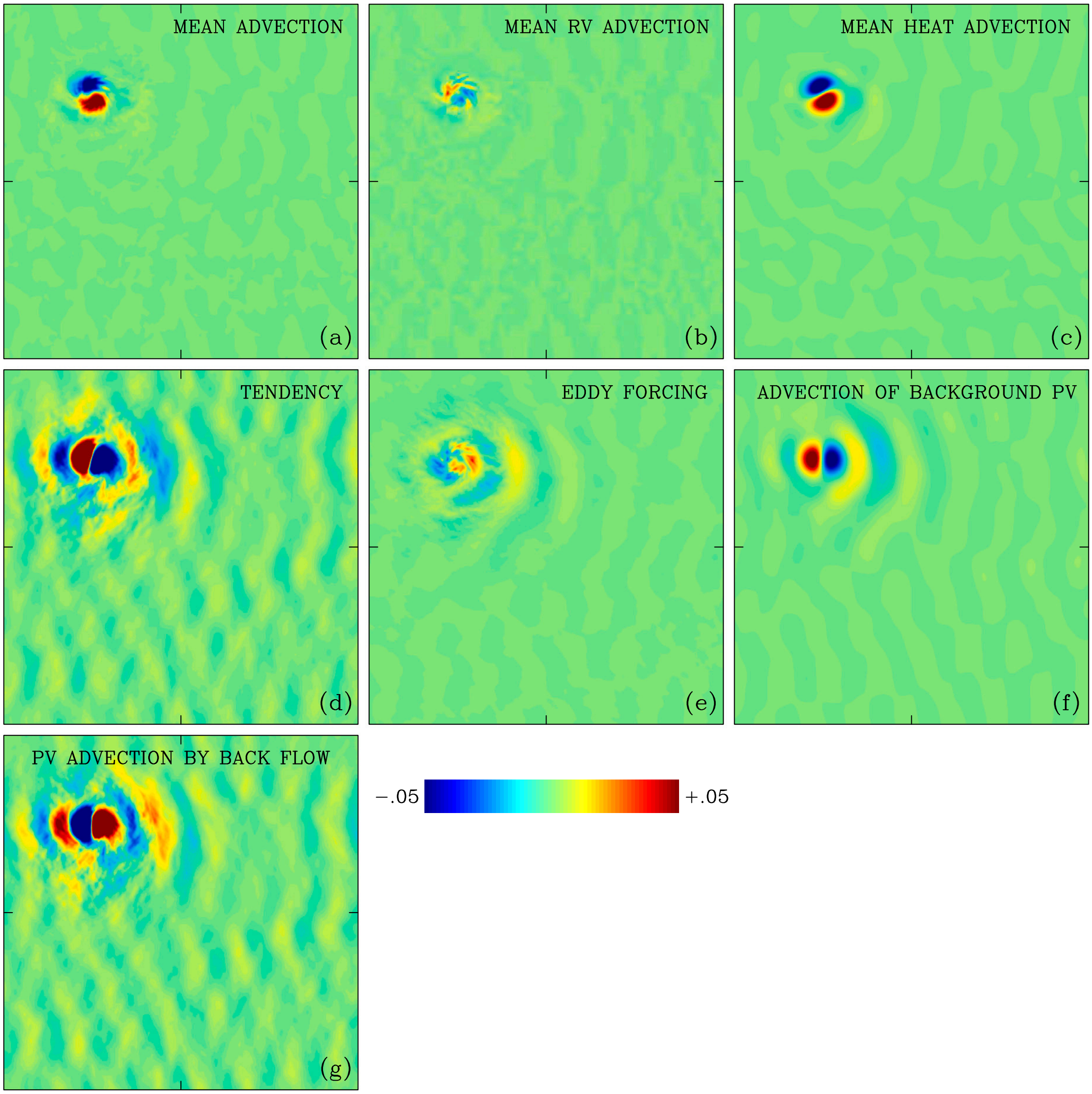

Fig. 12. The same set-up as in Fig. 10, but for the weak pulsar ($U_1 = -3$ cm s^{-1}). The upper-ocean fields are shown.

The key element of the problem set-up is presence of supercritical (i.e., linearly unstable), homogeneous westward background (WB) flow with vertical shear and the corresponding negative background potential vorticity (PV) gradient in the upper layer. An important conclusion of our study is that unstable background ocean circulation needs to be accounted for as one of the key factors affecting the vortex dynamics. Our approach is to use an intermediate-complexity quasi-geostrophic (QG) numerical model to compute statistically equilibrated model solutions, referred to as *baroclinic vortex pulsars (BVPs)* or simply "vortex pulsars", and to obtain and explore them for different physical parameters. Our definition of a vortex pulsar is that this a coherent self-propagating vortex-wave structure with 3 important properties: it is non-isolated, pulsating and asymmetric.

By solving initial-value problems and varying parameters, we discovered two distinct families of statistically equilibrated pulsars — referred to as "strong" and "weak", based on their vortex core intensities (strongly depending on γ and μ) — and we assume that some other pulsar types will be discovered in the future.[3] Note, that we could also refer to the families as "fast" and "slow", respectively, because the former family has systematically faster zonal propagation than the other one; in fact, except for extremely damped and nearly critical solutions, strong/weak pulsars are faster/slower than the WB flow. Having described these important characteristics, let us emphasize that the key distinction between the families is in terms of their nonlinear and quasi-linear dynamical balances, respectively. The BVPs are fundamentally non-isolated coherent vortices, because they extract energy from the background circulation and stratification, and expel back into

[3] In particular, the self-amplifying hetons in [26] Sutyrin et al. (2021b) may be intensifying vortex pulsars.

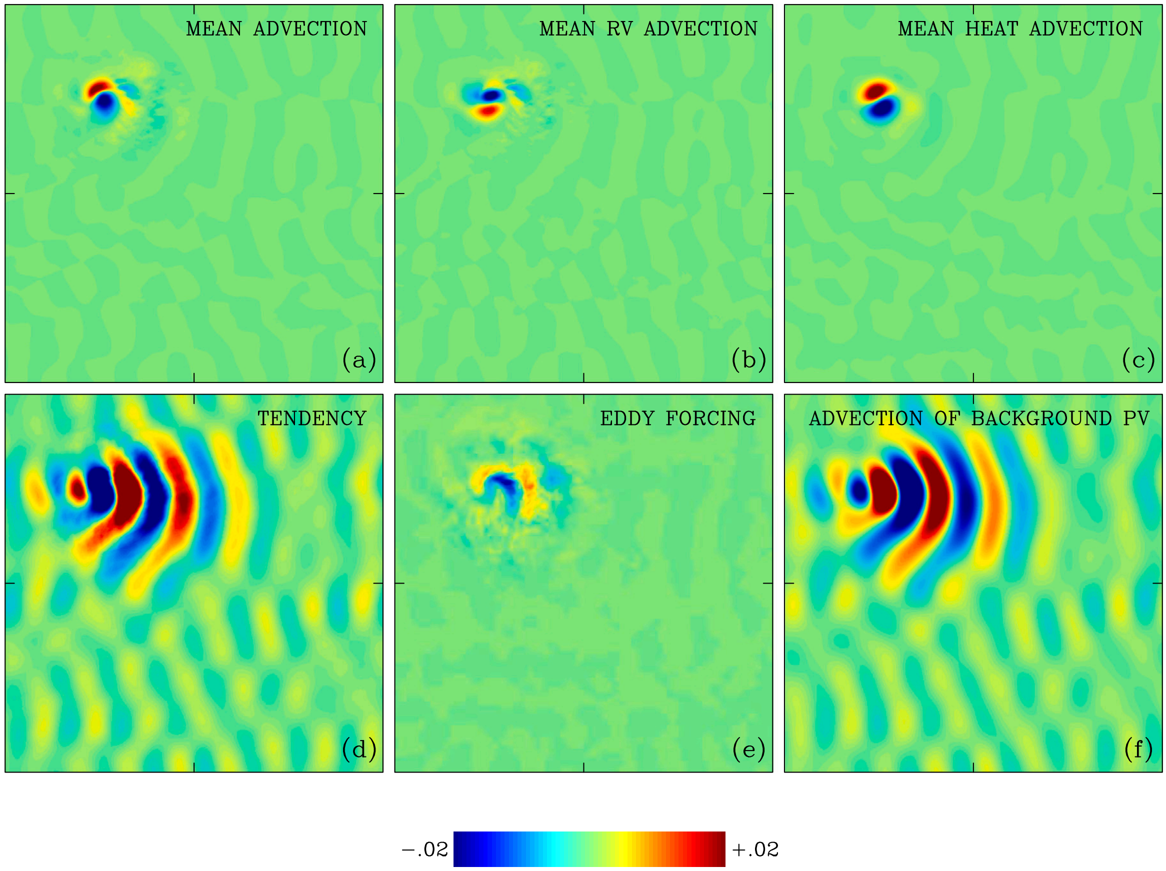

Fig. 13. The same set-up as in Fig. 11, but for the weak pulsar ($U_1 = -3$ cm s^{-1}). The deep-ocean fields are shown.

the environment pulses of excessive potential vorticity (PV), which accumulates due to down-gradient material propagation. In the BVPs the main vortex core in the upper layer is accompanied by the Rossby wave wake with the predominantly opposite-sign deep-ocean PV anomaly, which is horizontally shifted away from the upper-ocean core. This creates the dipolar pattern needed for the pulsar self-propagation (see also inviscid analytical approximation of the wake for marginally stable shear [25] Sutyrin et al. (2021a)). The first author hypothesizes that most of the oceanic mesoscale vortices in westward flows are weak pulsars, but such rare intense vortices as the Gulfstream and Agulhas rings are strong pulsars — the way to verify this from the observational or modeling data is by analyzing the involved dynamical balances. The second author does not see enough evidence collected so far for making this hypothesis.

Strong pulsar has relatively more intense upper-ocean core, whereas weak pulsar has relatively more intense wake. Both types of BVPs are asymmetric, nonstationary, and propagate systematically northwestward (having cyclonic core), because of the asymmetry related to the wake, and strong BVPs propagate faster and at steeper angles to latitudes. Both BVP families (and more so the weak one) are characterized by large vertical tilts, that is, by horizontal distances of several Rd_1 between the upper- and lower-layer main PV anomalies. Strong family is also characterized by much larger heat anomaly and significantly more intense energy uptake from the background shear. It is also important that in the westward flow, the background upper-ocean PV decreases northward providing an amplification mechanism for the PV anomaly, and this process is balanced mostly by the PV expulsion. We refer to this as vortex pulsar ventilation process. To provide the work needed for ventilation and to balance out energy dissipation, vortex pulsars persistently extract energy from the pool of available potential energy contained in the background tilted isopycnals, which are related to vertical shear through the thermal wind balance. The main dynamical distinction between the BVP families comes from their time-mean dynamical balance in the co-moving frame of reference. Weak pulsar tends to run against the background flow, in the sense that its main balance is between the tendency term and PV advection by the background flow; whereas, strong pulsar speeds over the background flow and, therefore, adds to the above balance its own time-mean flow advection. Weak pulsars have nearly linear dynamical balance, thus, suggesting that this flow feature can be viewed as weakly nonlinear Rossby waves packet. Strong pulsars have nonlinear time-mean advection entering the leading balance, thus, confirming that they are strongly nonlinear flow features.

Despite the vortex research topic being an old one, even classical, and despite many interesting results accumulated over the decades, there are many quests still remaining without complete answers; let us name some of them. Mechanisms of initial generation and adjustment towards long-lived states, not necessarily circular, as well as taxonomy of existing and possible vortex states remains incomplete. Further understanding is needed for vortex stability and instabilities, propagation characteristics, temporal variability, pairwise (and even groupwise) vortex interactions, radiation of inertia-gravity waves, long-range material transport and vortex-ventilating material exchanges with surrounding fluid. Perhaps, the least understood aspect are interactions between vortices and large-scale, background circulation and stratification patterns, which provide living environment for the vortices. Some

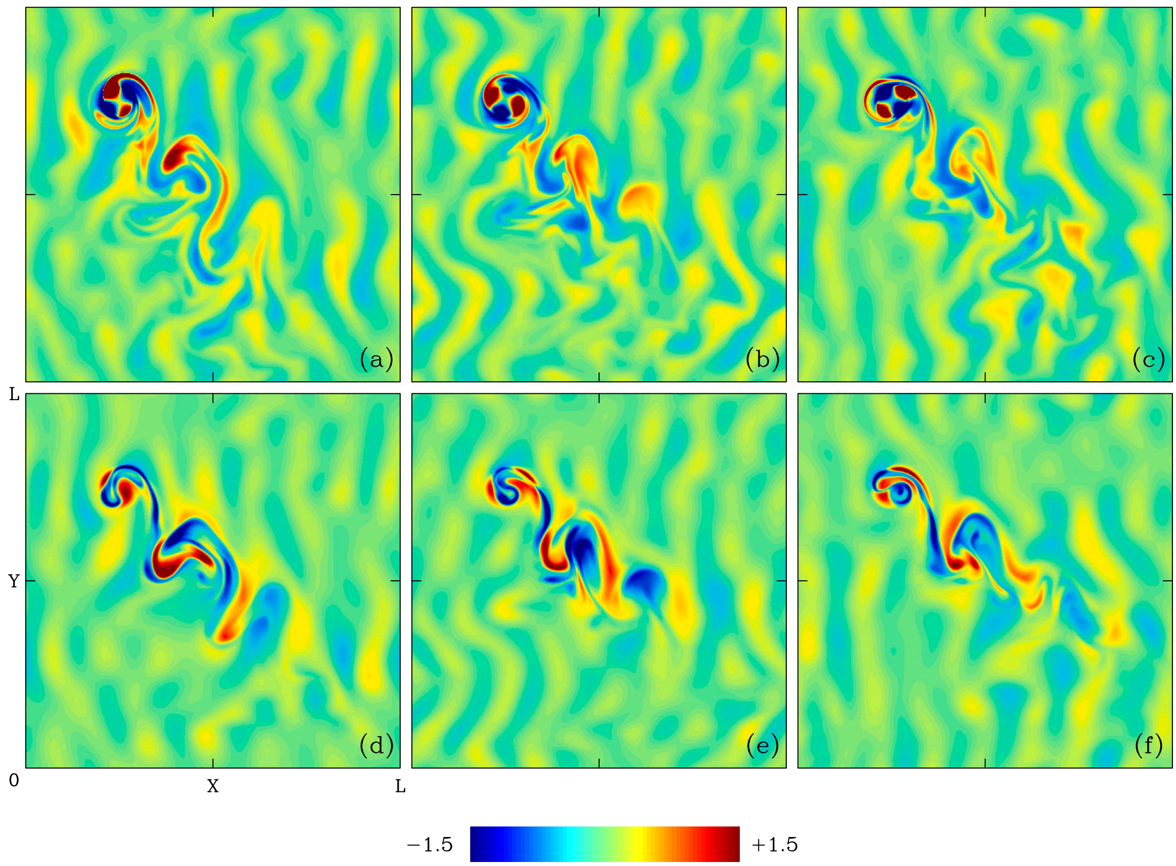

Fig. 14. Snapshots of the vortex pulsar perturbations corresponding to Fig. 1, from which the time-mean strong vortex pulsar (Fig. 5) was subtracted. Shown is PV anomaly in the (upper row of panels) upper ocean and (lower row) deep ocean. Units are 10^{-5} s^{-1}. Note cyclonically rotating quadrupole in the vortex pulsar core.

progress has been made for zonal flows with vertical shear, but most of the oceanic flows have non-zonal components, making them always unstable, as well as they have horizontal shears that can supply vortices with kinetic energy.

Our study can be viewed as a convenient platform and starting point for many future research extensions; let us mention some of them. First of all, viewing mesoscale oceanic eddies as vortex pulsars needs confirmation from analyses of the observations, and this, in turn, requires observational focus on specific properties, such as dynamical balances, PV exchange, and energy transfer from the background. Extra physics, which is expected to modify vortex pulsars, can be systematically added to the hierarchy of future models. In particular, the background flow can be taken nonzonal, jet-like, and even three-dimensional; sloping or sinusoidal bottom topography can be easily added; high vertical resolution can be employed for resolving details of the vertical BVP structure, as well as more realistic vertical shears. Both stable and unstable steady vortex states can be searched for by the Newton–Raphson methodology, though it is not guaranteed that they exist. Linear stability of vortex pulsars can be explored via directly solving the corresponding (very large) eigenproblem (e.g., as in [37] Shevchenko et al. 2016; [38] Davies et al. 2024). More advanced analyses are needed for the BVP structure and spatio-temporal variability patterns. For example, vortex pulsar solutions can be projected on the normal Rossby wave modes of the westward background flows ([35] Berloff and Kamenkovich 2013; [36] Haigh and Berloff 2020), for better understanding roles played by the Rossby waves in the dynamics of vortex pulsars. Going beyond quasigeostrophic asymptotics into primitive equations is well motivated but computationally expensive. Detailed Lagrangian analyses are needed to understand material ventilation of the vortex core, that maintains the PV balance. Studying sensitivity of the pulsars to the bottom friction and topography should be prioritized, as our results show that there are strong dependencies there, especially for the weak pulsars. Finally, considering ensembles of interacting vortex pulsars, that is, vortex gases, would shed light on various vortex-vortex interactions and their cumulative effects.

CRediT authorship contribution statement

Pavel Berloff: Writing – original draft, Visualization, Validation, Resources, Methodology, Investigation, Formal analysis, Data curation, Conceptualization. **Georgi G. Sutyrin:** Writing – original draft, Methodology, Investigation, Conceptualization.

Declaration of competing interest

The authors declare that they have no known competing financial interests or personal relationships that could have appeared to influence the work reported in this paper.

Data availability

Data will be made available on request.

Acknowledgments

Critical comments and helpful suggestions from Jim McWilliams, Timour Radko, Mikhail Sokolovskiy, Matt Crowe and an anonymous reviewer are greatly appreciated. PB was supported by the Moscow Center for Fundamental and Applied Mathematics (supported by the agreement 075-15-2022-1624 with the Ministry of Education and Science of the Russian Federation). GS was supported by the U.S. National Science Foundation (NSF-OCE-1828843).

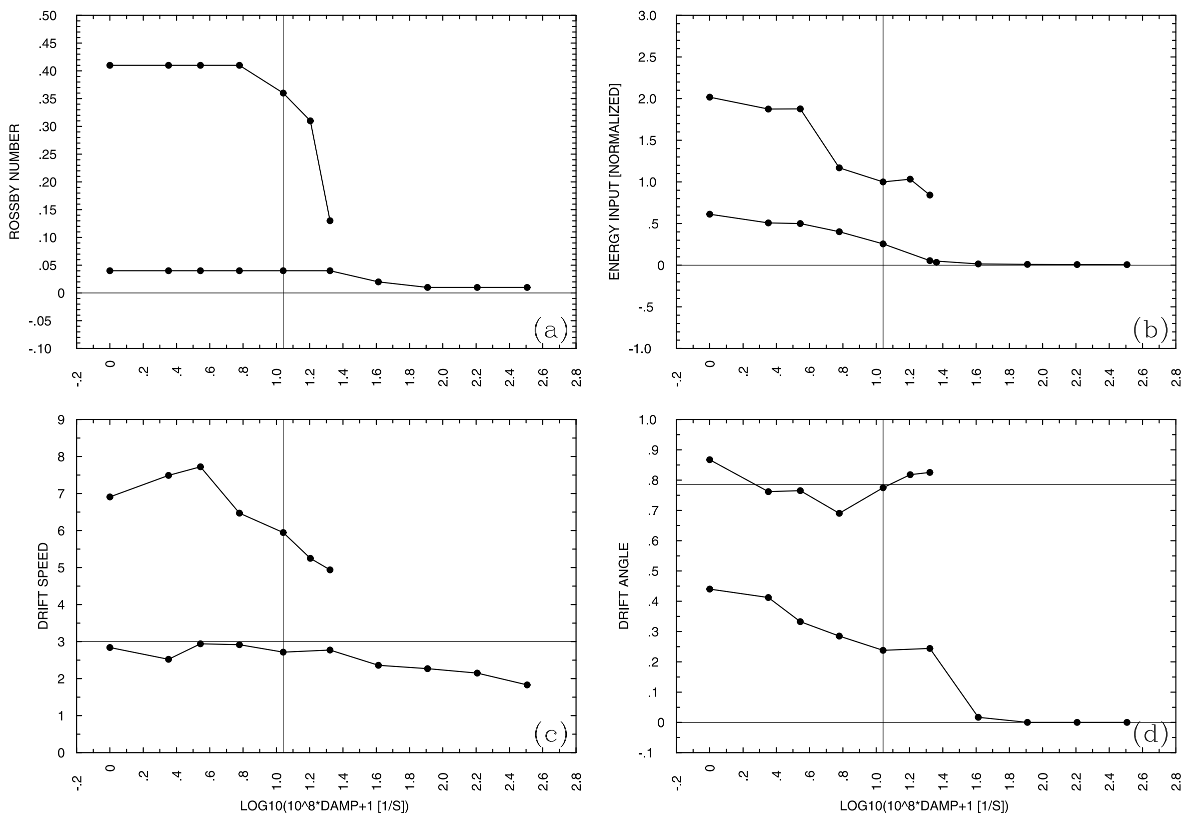

Fig. 15. Dependences of vortex pulsar characteristics on the far-field damping parameter δ. Note, that abscissa has logarithmic scale and values of δ are shifted in order to be able to show $\delta = 0$. Vertical lines on the panels indicate the reference value.

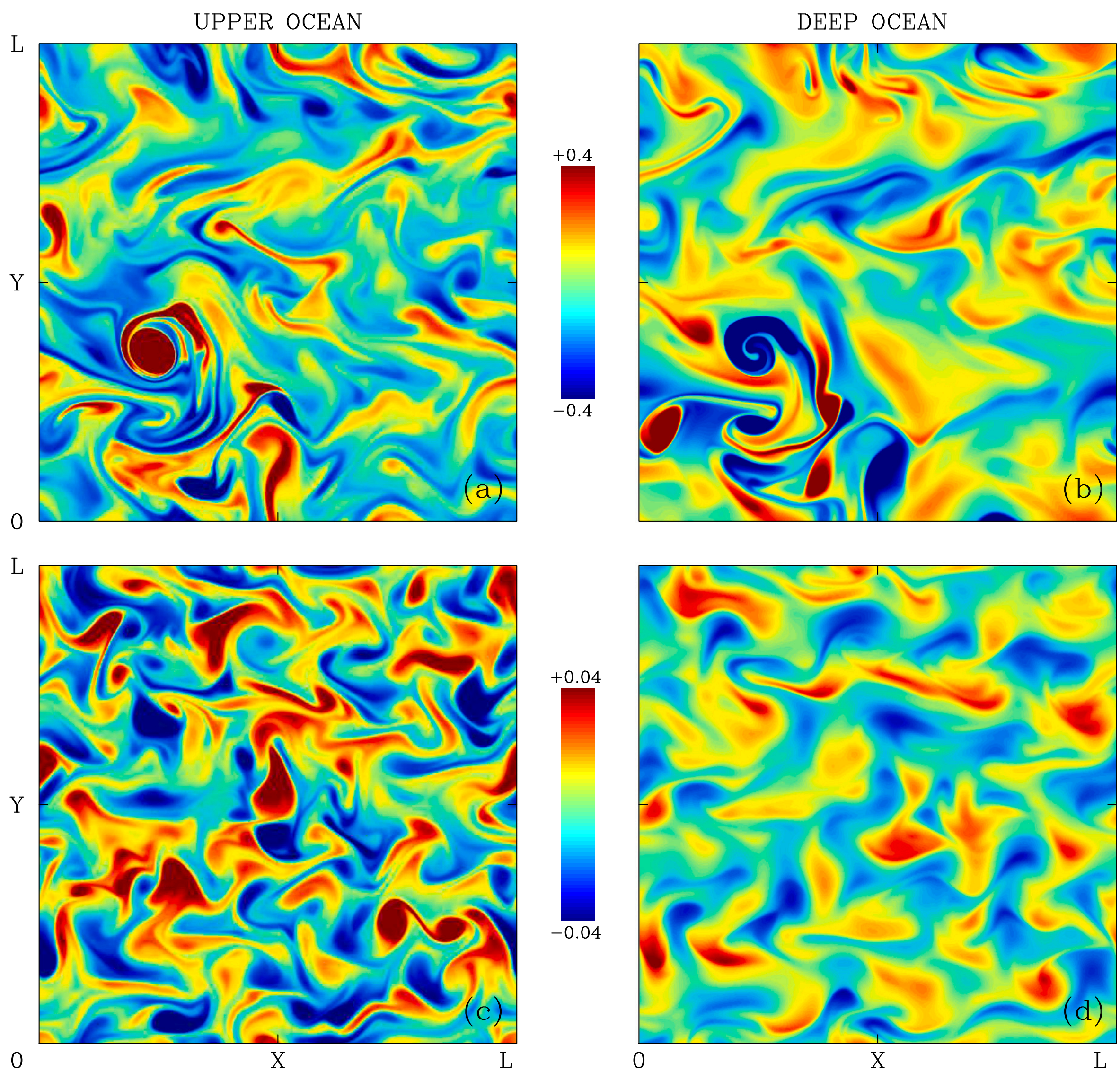

Fig. 16. Instantaneous snapshots of the reference strong and weak pulsars, except for the peripheral damping, which is turned off. Upper/lower panels correspond to the strong/weak pulsar; left/right panels correspond to the top/bottom layers. Shown are the PV anomalies normalized by the maximum values in the upper-ocean fields. Position of the strong pulsar core is well seen, whereas position of the weak pulsar core, which is roughly at $x = 3/4$ and $y = 1/4$, can be easily confused with the other anomalies of similar intensity. Comparison of this Figure with Figs. 1 and 2 illustrates importance of the peripheral damping in cleaning up fluctuations and eddies surrounding the pulsars in focus.

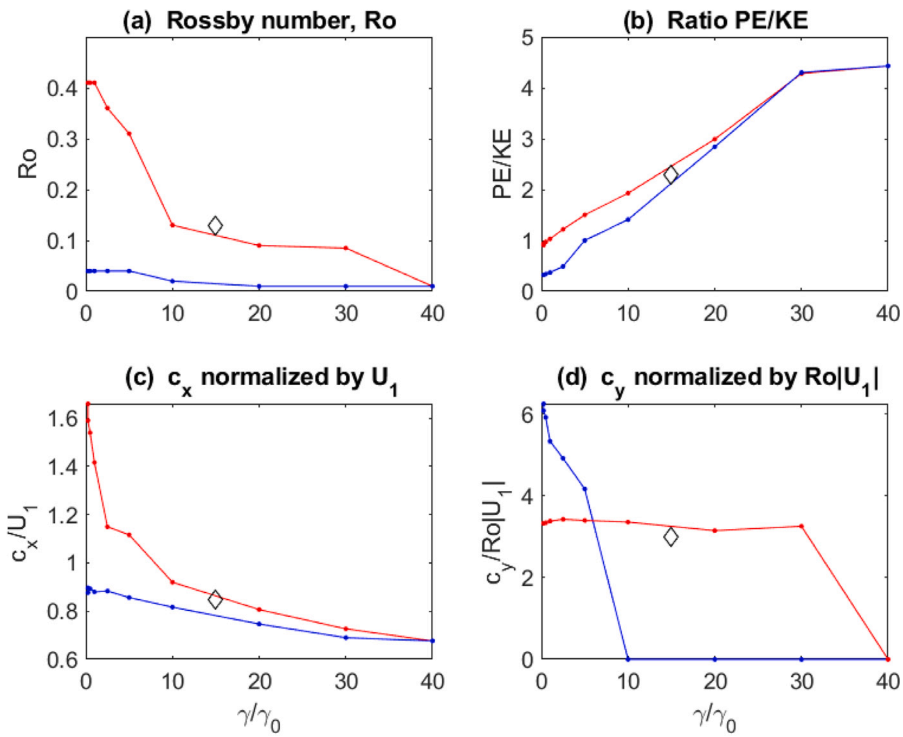

Fig. 17. Dependences of pulsar characteristics on the bottom friction parameter γ/γ_0: (a) the Rossby number; (b) the potential-to-kinetic energy ratio PE/KE; (c) the zonal propagation speed normalized by U_1; (d) the ratio of the meridional propagation speed to $Ro|U_1|$. Strong (red) and weak (blue) pulsar families are shown together. The diamonds correspond to the strongest vortex for $\gamma/\gamma_0 = 15, \nu/\nu_0 = 1.2, \epsilon = 1$ analyzed in [26] (Sutyrin et al. 2021b).

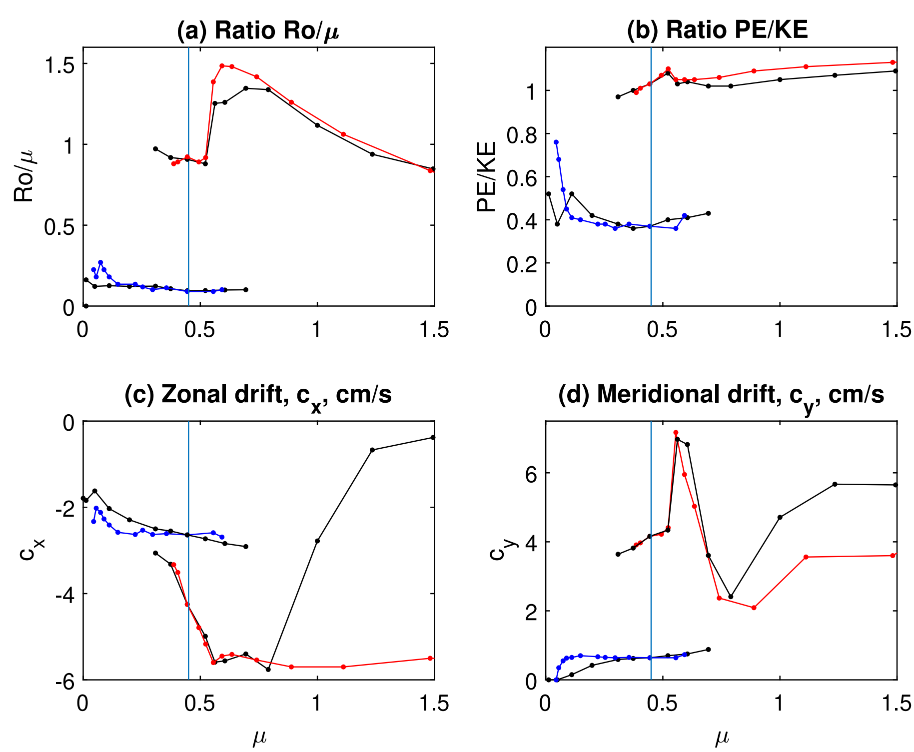

Fig. 18. The vortex pulsar characteristics for various ν and U_1 values and their combination μ. Strong and weak branches of pulsars are clearly seen; solution for each branch is illustrated by its set of dots connected by the piece-wise linear curves. Variations of ν are shown for strong (red) and weak (blue) pulsars, whereas variations of ϵ are shown by black curve. Vertical lines on the panels indicate the reference value of $\mu = 0.45$ for which the equilibrated states were considered in Section 3. (a) Ratio Ro/μ; (b) ratio of potential and kinetic energies; (c) zonal component c_x of the pulsar propagation velocity; (d) meridional component c_y of the pulsar propagation velocity.

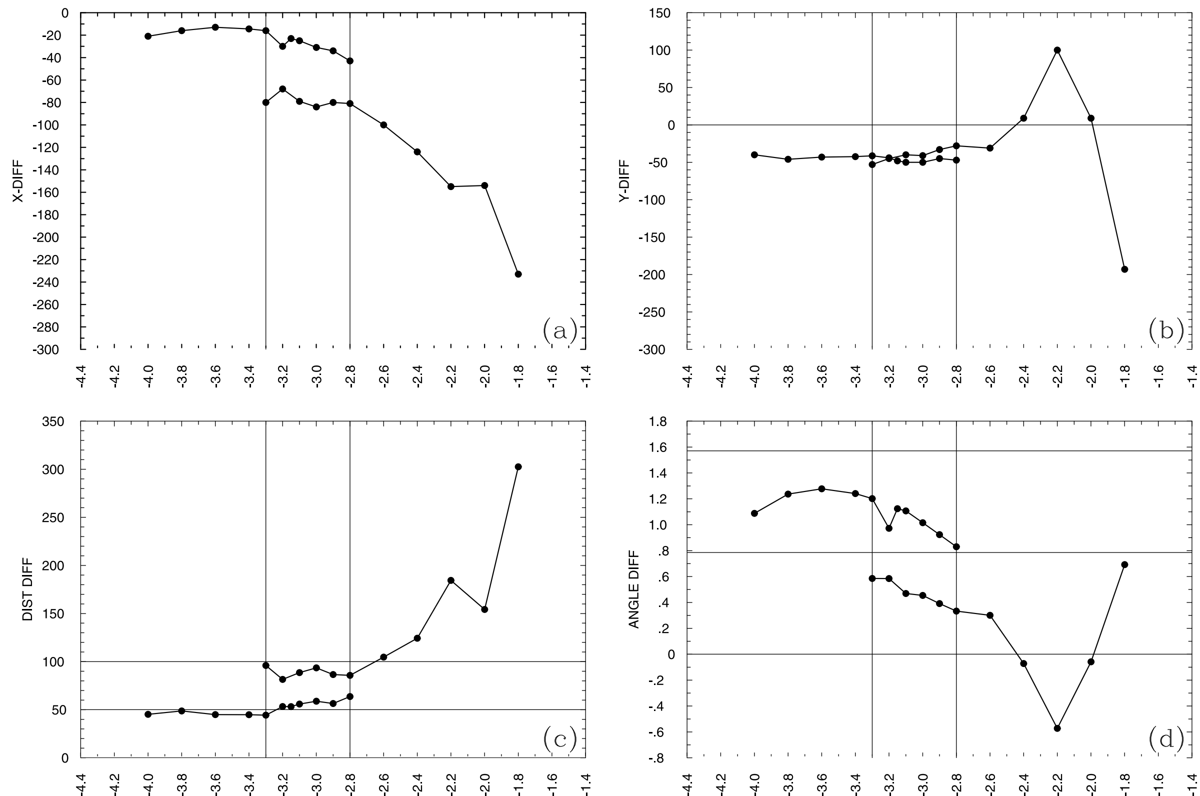

Fig. 19. Dependences of the vertical tilt characteristics of vortex on the background-flow velocity parameter U_1; two distinct branches are clearly seen and the dependencies can be compared with those in Fig. 18. The tilt is described in terms of the position of the deep-ocean negative PV extremum relative to the upper-ocean positive PV extremum; this can be viewed as either 2D vector or distance combined with angle. (a) distance between the extrema along zonal direction (negative sign implies that the deep-ocean PV anomaly is to the east of the upper-ocean one); (b) distance between the extrema along meridional direction (negative sign implies that the deep-ocean PV anomaly is to the north of the upper-ocean one); (c) full distance between the extrema, that is, vortex tilt (horizontal straight lines indicate $2Rd_1$ and $4Rd_1$ values); (d) angle of the tilt direction relative to zonal axis (positive angle implies that the deep-ocean vortex is to the north-east from the upper-ocean one; horizontal straight lines indicate $0, \pi/4, \pi/2$ angles). Two vertical lines on the panels indicate the range of U_1 for which two branches co-exist.

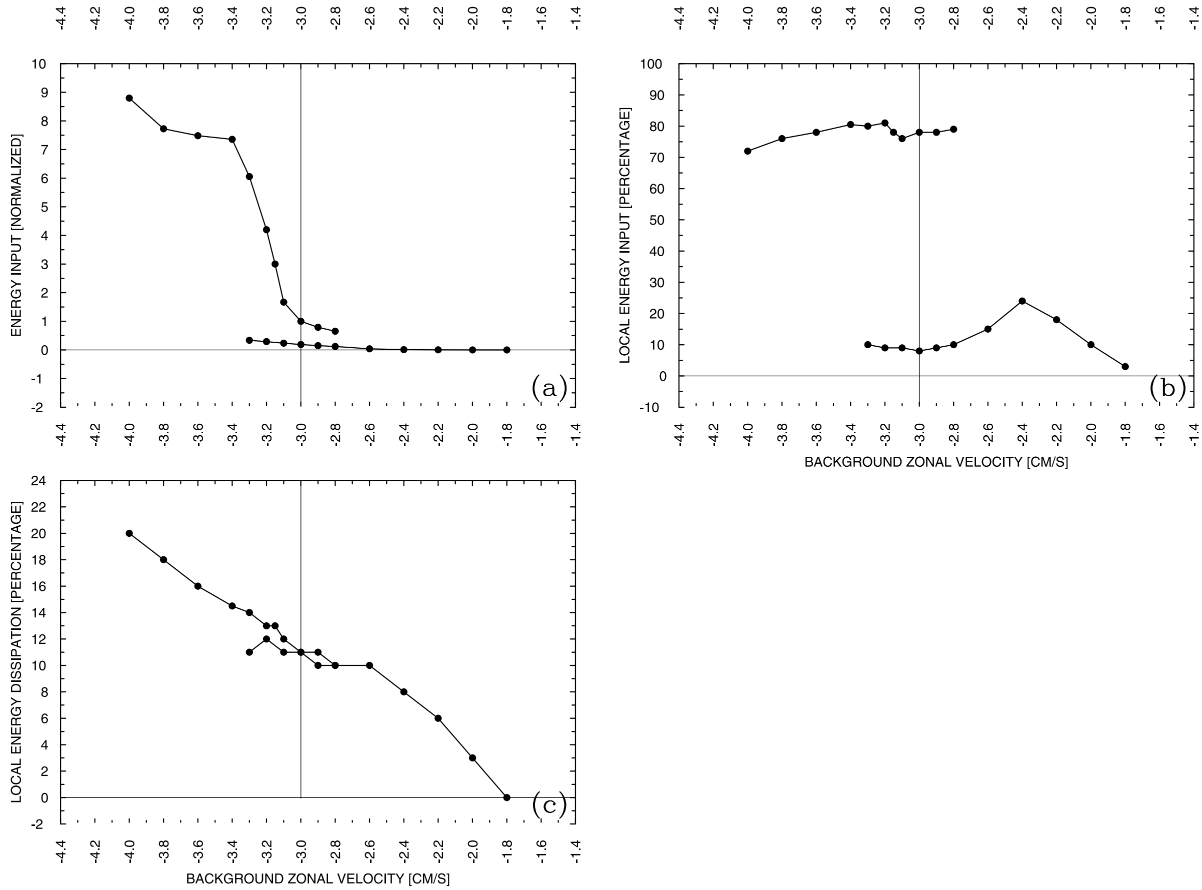

Fig. 20. Dependencies of the pulsar energy characteristics on U_1. (a) total energy input from the background shear (the values are normalized so that input for the reference strong solution is unity); (b) local energy input as percentage of the total energy input (here, radius of the local circle is $4Rd_1$); (c) local energy dissipation as percentage of the local energy input. Vertical lines on the panels indicate U_1 for the reference solutions.

References

[1] J. McWilliams, J. Weiss, Anisotropic geophysical vortices, Chaos 4 (1994) 305–311.
[2] T. Dowling, E. Spiegel, Stellar and jovian vortices, Ann. New York Acad. Sci. 617 (1990) 190–216.
[3] J. McWilliams, The emergence of isolated coherent vortices in turbulent flow, J. Fluid Mech. 146 (1984) 21–43.
[4] G. Brown, A. Roshko, On density effects and large structures in turbulent mixing layers, J. Fluid Mech. 64 (1974) 775–816.
[5] V. Larichev, G. Reznik, On two-dimensional solitary Rossby waves, Dokl. Akad. Nauk 231 (1976) 1077–1079.
[6] J. McWilliams, The nature and consequences of oceanic eddies, in: M. Hecht, H. Hasumi (Eds.), Eddy-Resolving Ocean Modeling, in: AGU Monograph, vol. 13, 2008, pp. 1–147.
[7] D. Chelton, M. Schlax, R. Samelson, Global observations of nonlinear mesoscale eddies, Prog. Oceanogr. 91 (2011) 167–216.
[8] G. Haller, A. Hadjighasem, F. Huhn, Defining coherent vortices objectively from the vorticity, J. Fluid Mech. 795 (2016) 136–173.
[9] G. Chen, G. Hana, X. Yanga, On the intrinsic shape of oceanic eddies derived from satellite altimetry, Ocean Remote Sens. Environ. 228 (2019) 75–89.
[10] G.G. Sutyrin, The importance of being asymmetric for geophysical vortices, Symmetry 15 (2023) 2204.
[11] H. Wang, H. Qiu, B. Liu, Z. Zhang, Doubling of surface oceanic meridional heat transport by non-symmetry of mesoscale eddies, Nature Commun. 14 (2023) 5460.
[12] J. Davies, G.G Sutyrin, P. Berloff, On the spontaneous symmetry breaking of eastward propagating dipoles, Phys. Fluids 35 (2023) 041707.
[13] J. Davies, M. Sutyrin, G.G. Crowe, P. Berloff, Deformation and destruction of north-eastward drifting dipoles, Phys. Fluids 35 (2023) 116601.
[14] J. McWilliams, G. Flierl, On the evolution of isolated, nonlinear vortices, J. Phys. Oceanogr. 9 (1979) 1155–1182.
[15] G. Sutyrin, G. Flierl, Intense vortex motion on the beta plane: development of the beta gyres, J. Atmos. Sci. 51 (1994) 773–790.
[16] G.G. Sutyrin, J. Hesthaven, J. Lynov, J. Rasmussen, Dynamical properties of vortical structures on the beta-plane, Fluid Mech. 268 (1994) 103–131.
[17] S. Lam, D. Dritschel, On the beta-drift of an initially circular vortex patch, J. Fluid Mech. 436 (2001) 107–129.
[18] J. Early, R. Samelson, D. Chelton, The evolution and propagation of quasigeostrophic ocean eddies, J. Phys. Oceanogr. 41 (2011) 1535–1555.
[19] G.G. Sutyrin, T. Radko, Why the most long-lived oceanic vortices are found in the subtropical westward flows, Ocean Model. 161 (2021) 101782.
[20] N. Phillips, Energy transformations and meridional circulations associated with simple baroclinic waves in a two level,quasi-geostrophic model, Tellus 6 (1954) 273–286.
[21] B. Gallet, R. Ferrari, The vortex gas scaling regime of baroclinic turbulence, Proc. Natl. Acad. Sci. USA 117 (2020) 4491–4497.
[22] P. Berloff, T. Karabasov, S. Farrar, I. Kamenkovich, On latency of multiple zonal jets in the oceans, J. Fluid Mech. 686 (2011) 534–567.
[23] P. Sangra, et al., The canary Eddy corridor: A major pathway for long-lived eddies in the subtropical north atlantic, Deep-Sea Res. I 56 (2009) 2100–2114.
[24] A. Dilmahamod, B. Aguiar-Gonzalez, P. Penven, C. Reason, W. de Ruijter, N. Malan, J. Hermes, SIDDIES corridor: A major east–west pathway of long-lived surface and subsurface eddies crossing the subtropical south Indian Ocean, J. Geophys. Res. Oceans 123 (2018) 5406–5425.
[25] G.G. Sutyrin, T. Radko, J. Nycander, Steady radiating baroclinic vortices in vertically sheared flows, Phys. Fluids 33 (2021) 031705.
[26] G.G. Sutyrin, T. Radko, J. McWilliams, Self-amplifying hetons in vertically sheared geostrophic turbulence, Phys. Fluids 33 (2021) 101705.
[27] N. Hogg, H. Stommel, The heton an elementary interaction between discrete baroclinic geostrophic vortices, and its implications concerning Eddy heat-flow, Proc. R. Soc. Lond. Ser. A 397 (1985) 1–20.
[28] V. Gryanik, M. Sokolovskiy, J. Verron, Dynamics of heton-like vortices, Regul. Chaotic Dyn. 11 (3) (2006) 383–434.
[29] T. Radko, J. McWilliams, G.G. Sutyrin, Equilibration of baroclinic instability in westward flows, J. Phys. Oceanogr. 52 (2022) 21–38.
[30] G.G. Sutyrin, T. Radko, J. McWilliams, Contrasting Eddy-driven transport in baroclinically unstable eastward currents and subtropical return flows, Phys. Fluids 34 (2022) 126605.
[31] L. Gulliver, T. Radko, On the propagation and translational adjustment of isolated vortices in large-scale shear flows, J. Phys. Oceanogr. 52 (2022) 1655–1675.

[32] M. Melander, N. Zabusky, J. McWilliams, Symmetric vortex merger in two dimensions: causes and conditions, J. Fluid Mech. 195 (1988) 303–340.
[33] S. Karabasov, P. Berloff, V. Goloviznin, CABARET in the ocean gyres, Ocean Model. 30 (2009) 155–168.
[34] I. Shevchenko, P. Berloff, Multi-layer quasi-geostrophic ocean dynamics in Eddy-resolving regimes, Ocean Model. 94 (2015) 1–14.
[35] P. Berloff, I. Kamenkovich, On spectral analysis of mesoscale eddies part I. Linear analysis, J. Phys. Oceanogr. 43 (2013) 2505–2527.
[36] M. Haigh, P. Berloff, Rossby waves and zonal momentum redistribution induced by localised forcing in the rotating shallow-water model, J. Fluid Mech. 885 (2020) A43.
[37] I. Shevchenko, P. Berloff, D. Guerrero-Lopez, J. Roman, On low-frequency variability of the midlatitude ocean gyres, J. Fluid Mech. 795 (2016) 423–442.
[38] J. Davies, P. Shevchenko, I. Berloff, G.G. Sutyrin, Linear instability and weakly nonlinear effects in eastward dipoles, Phys. D. 460 (2024) 134068.